The Astrophysical Journal, 864:45 (15pp), 2018 September 1 https://doi.org/10.3847/1538-4357/aad2df

Results from a Systematic Survey of X-Ray Emission from Hydrogen-poor Superluminous SNe

R. Margutti[1], R. Chornock[2], B. D. Metzger[3], D. L. Coppejans[1], C. Guidorzi[4], G. Migliori[5], D. Milisavljevic[6], E. Berger[6], M. Nicholl[6], B. A. Zauderer[7], R. Lunnan[8], A. Kamble[6], M. Drout[9,10], and M. Modjaz[7]
[1] Center for Interdisciplinary Exploration and Research in Astrophysics (CIERA) and Department of Physics and Astronomy, Northwestern University, Evanston, IL 60208, USA
[2] Astrophysical Institute, Department of Physics and Astronomy, 251B Clippinger Lab, Ohio University, Athens, OH 45701, USA
[3] Columbia Astrophysics Laboratory, Columbia University, Pupin Hall, New York, NY 10027, USA
[4] Department of Physics and Earth Science, University of Ferrara, via Saragat 1, I-44122, Ferrara, Italy
[5] Laboratoire AIM (CEA/IRFU—CNRS/INSU—Universite Paris Diderot), CEA DSM/SAp, F-91191 Gif-sur-Yvette, France
[6] Harvard-Smithsonian Center for Astrophysics, 60 Garden Street, Cambridge, MA 02138, USA
[7] Center for Cosmology and Particle Physics, New York University, 4 Washington Place, New York, NY 10003, USA
[8] Department of Astronomy, California Institute of Technology, 1200 East California Boulevard, Pasadena, CA 91125, USA
[9] Carnegie Observatories, 813 Santa Barbara Street, Pasadena, CA 91101, USA
Received 2017 April 18; revised 2018 June 23; accepted 2018 June 27; published 2018 August 29

Abstract

We present the results from a sensitive X-ray survey of 26 nearby hydrogen-poor superluminous supernovae (SLSNe-I) with *Swift*, *Chandra,* and *XMM*. This data set constrains the SLSN evolution from a few days until ∼2000 days after explosion, reaching a luminosity limit $L_x \sim 10^{40}$ erg s^{-1} and revealing the presence of significant X-ray emission possibly associated with PTF 12dam. No SLSN-I is detected above $L_x \sim 10^{41}$ erg s^{-1}, suggesting that the luminous X-ray emission $L_x \sim 10^{45}$ erg s^{-1} associated with SCP 60F6 is not common among SLSNe-I. We constrain the presence of off-axis gamma-ray burst (GRB) jets, ionization breakouts from magnetar engines and the density in the sub-parsec environments of SLSNe-I through inverse Compton emission. The deepest limits rule out the weakest uncollimated GRB outflows, suggesting that *if* the similarity of SLSNe-I with GRB/SNe extends to their fastest ejecta, then SLSNe-I are either powered by energetic jets pointed far away from our line of sight ($\theta > 30°$), or harbor failed jets that do not successfully break through the stellar envelope. Furthermore, *if* a magnetar central engine is responsible for the exceptional luminosity of SLSNe-I, our X-ray analysis favors large magnetic fields $B > 2 \times 10^{14}$ G and ejecta masses $M_{\rm ej} > 3\ M_\odot$, in agreement with optical/UV studies. Finally, we constrain the pre-explosion mass-loss rate of stellar progenitors of SLSNe-I. For PTF 12dam we infer $\dot{M} < 2 \times 10^{-5}\ M_\odot$ yr^{-1}, suggesting that the SN shock interaction with an extended circumstellar medium is unlikely to supply the main source of energy powering the optical transient and that some SLSN-I progenitors end their lives as compact stars surrounded by a low-density medium similar to long GRBs and type Ib/c SNe.

Key words: stars: magnetars – stars: mass-loss – supernovae: general – X-rays: general

Supporting material: machine-readable table

1. Introduction

Superluminous supernovae (SLSNe) are among the most luminous known stellar explosions in the universe. Only recently recognized as a class, in 2009 (Chomiuk et al. 2011; Quimby et al. 2011c), SLSNe reach optical-UV luminosities $L > 7 \times 10^{43}$ erg s^{-1}, ∼10–100 more luminous than common SNe, and are likely associated with the death of massive stars. The source of energy powering their exceptional energy release is still debated (e.g., Gal-Yam 2012). The proposed energy sources include: (i) radioactive decay of large amounts of freshly synthesized ^{56}Ni ($M_{\rm Ni} \gtrsim 5\ M_\odot$), a signature of pair-instability explosions (as proposed for SN 2007bi, Gal-Yam et al. 2009); (ii) SN shock interaction with dense material in the environment (e.g., Smith & McCray 2007; Chevalier & Irwin 2011); and (iii) a magnetar central engine (e.g., Kasen & Bildsten 2010; Woosley 2010; Nicholl et al. 2013). The narrow features ($v \lesssim 100$ km s^{-1}) in the spectra of hydrogen-rich SLSNe like SN 2006gy clearly indicate that the interaction of the SN blast wave with the medium plays a role (e.g., Ofek et al. 2007; Smith & McCray 2007), while it is unclear if a single mechanism can power hydrogen-stripped SLSNe (i.e., SLSNe-I). Indeed, SLSN-I iPTF 13ehe has been interpreted as the combination of energy extracted from a magnetar central engine coupled with radiation from the radioactive decay of ∼2.5 $M_\odot$ of ^{56}Ni, and a late-time interaction of the SN shock with the medium (Yan et al. 2015; Wang et al. 2016b).

A number of independent lines of evidence support the idea that SLSNe-I might harbor an engine. Observations of SLSN-I host galaxies indicate a preference for low-metallicity environments, which inspired a connection with long gamma-ray bursts (GRBs, Lunnan et al. 2014; Leloudas et al. 2015b; Chen et al. 2017; Perley et al. 2016; see, however, Angus et al. 2016). Along the same line, Greiner et al. (2015) reported the detection of SN 2011kl associated with GRB 111209A (Kann et al. 2016) with color and luminosity properties that are reminiscent of SLSNe, and suggested that a magnetar central engine powered both the initial burst of γ-rays and the later optical/UV SN emission (Metzger et al. 2015). Milisavljevic et al. (2013) found links between the late-time emission properties of a subset of

[10] Hubble, Carnegie-Dunlap Fellow.

Table 1
Gold Sample

SN	z	d_L (Mpc)	Discovery Date (MJD)	Inferred Explosion Date (MJD)	NH_{MW} (10^{20} cm^{-2})	Instrument
SCP 06F6	1.189	8310	53787[a]	53767[b]	0.885	*XMM+CXO*
PTF 12dam	0.107	498	56037[a]	56022[c]	1.11	*Swift+CXO*
PS1-14bj	0.521	3012	56618[d]	56611[e]	1.71	*XMM*
SN 2015bn/PS15ae	0.1136	513.2	57014[f]	57013[g]	2.37	*Swift+XMM*

Notes.
[a] From Levan et al. (2013).
[b] The time of the peak is MJD 53872. The rise-time is ∼50 days in the rest-frame (Barbary et al. 2009).
[c] The light curve reached maximum light on MJD 56088 and the rest-frame rise-time is ∼60 days (Nicholl et al. 2013).
[d] From Lunnan et al. (2016).
[e] Lunnan et al. (2016) estimate a peak time on MJD 56801.3 and a rest-frame rise-time $\gtrsim$125 days.
[f] From Nicholl et al. (2016b).
[g] The SN reached *r*-band maximum light on MJD 57102 (Nicholl et al. 2016b). The rise-time inferred by Nicholl et al. (2016b) is ∼80 days in the rest-frame.

energetic, slow-evolving supernovae, and the superluminous SN 2007bi. They suggested that a single, possibly jetted, explosion mechanism may unify all of these events that span $-21 \leqslant M_B \leqslant -17$ mag.[11] Additionally, nebular spectroscopic studies by Nicholl et al. (2016b) revealed similarities between the SLSN-I 2015bn and SN 1998bw, associated with GRB 980425, suggesting that the cores of their massive progenitors shared a similar structure at the time of collapse. In another source, SLSN-I Gaia 16apd, Nicholl et al. (2017) further demonstrated that the luminous excess of UV emission originates from a central source of energy, rather than reduced UV absorption or shock interaction with a thick medium (see, however, Yan et al. 2017). Finally, luminous X-ray emission has been detected at the location of the SLSN-I SCP 06F6 (Gänsicke et al. 2009) with a luminosity $L_x \sim 10^{45}$ erg s^{-1} $\sim$ 70 days (rest-frame) after the explosion (Levan et al. 2013). At this epoch, SCP 06F6 even outshines GRBs by a large factor, suggesting the presence of a still-active central engine that manifests itself through very luminous and long-lasting X-ray emission (Levan et al. 2013; Metzger et al. 2015). Before our efforts, SCP 06F6 was the only SLSN-I for which an X-ray source was detected at a location consistent with the optical transient.

These observational results suggest a connection between SLSNe-I and engine-driven SNe. However, it is not yet known how the properties of the engines (successful jet? relativistic ejecta? collimated or spherical central-engine-powered outflow?), progenitor stars, and circumstellar environments would compare. Here, we present the results from a systematic search for X-ray emission from SLSNe-I both at early and at late times, which directly depends on the properties of the immediate environment and central engine (if any). The direct detection of the stellar progenitors of SLSNe-I in pre-explosion optical images is not possible due to their large distances ($z \geqslant 0.1$). Sampling the circumstellar density profile in the closest environment is thus the most direct probe of their progenitors and their recent mass-loss history before stellar death.

The data set that we present here includes the deepest X-ray observations of SLSNe-I with *Swift*, *XMM,* and the *Chandra X-ray Observatory* (*CXO*), extending from the time of discovery until ∼2000 days (rest-frame) after explosion, and led to the discovery of X-ray emission at the location of the slowly evolving SLSN-I PTF 12dam. These observations, described in Section 2, indicate that superluminous X-ray emission similar to what was observed in association with SCP 06F6 is not common in SLSNe-I (Section 3) and allow us to place meaningful constraints on the environment density at the SLSN site (Section 4). We constrain the properties of central engines in SLSNe-I in Section 5 by investigating the presence of late-time X-ray re-brightenings that can either be due to emission from off-axis collimated relativistic outflows similar to GRBs, or to the ionization breakouts from magnetar central engines (Metzger et al. 2014). Conclusions are drawn in Section 6.

2. X-Ray Observations and Analysis

Since 2011, we routinely followed up all publicly announced nearby ($z \lesssim 0.5$) SLSNe-I with *Swift*-XRT with a series of observations acquired between the time of discovery and ∼360 days (rest-frame) after explosion. For a subset of events we acquired deep X-ray observations with dedicated programs on the *CXO* and *XMM-Newton*. Additionally, we searched the *Swift*-XRT, *CXO*, and *XMM* archives for serendipitous or unpublished observations of SLSNe-I discovered before 2016 May. Our final sample consists of 26 SLSNe-I discovered between 2006 and 2016 May. The data set covers the time range between ∼days after explosion until ∼2000 days (rest-frame) and comprises ∼700 hr of observations. We update the X-ray observations of the sample of 11 SLSNe-I from Levan et al. (2013) with the most recent data[12] and we add 15 new SLSNe-I. Inserra et al. (2017) presented a selection of *Swift*-XRT observations of three SLSNe. The much longer temporal baseline and better sensitivity of the X-ray data set presented here allow us to constrain the environments and the properties of central engines possibly powering the SLSN emission.

We divide our sample into three groups: the "gold sample" (Table 1) contains 4 SLSNe-I with X-ray detections or well-sampled optical bolometric light curve and deep X-ray limits obtained with *XMM* or the *CXO*. The "bronze sample" contains 12 SLSNe-I with sparser optical data but with good *Swift*-XRT

[11] N ote that Soker (2017 and references therein) go a step further and interestingly propose that all core-collapse SNe are in fact jet-driven explosions.

[12] Note that PTF 11dsf and CSS121015, included by Levan et al. (2013) in the sample of SLSNe-I, are in fact H-rich events (see Benetti et al. 2014; Perley et al. 2016). Additionally, for PTF 11dsf an AGN interpretation cannot be ruled out (Perley et al. 2016). For these reasons, we do not include these two events in our sample of SLSNe-I.

Table 2
Bronze Sample

SN	z	d_L (Mpc)	Discovery Date (MJD)	Inferred Explosion Date (MJD)	NH_{MW} (10^{20} cm^{-2})	Instrument
PTF 09cnd	0.258	1317	55025[a]	55006[b]	2.20	*Swift+XMM*
SN 2010gx	0.230	1156	55260[a]	55251[c]	3.28	*Swift*
SN 2010kd	0.101	468	55453[a]	55398[d]	2.32	*Swift*
SN 2011ke	0.143	682	55650[a]	55649[e]	1.27	*Swift+CXO*
SN 2012il	0.175	851	55926[a]	55919[e]	2.38	*Swift*
iPTF 13ehe	0.3434	1833	56621[f]	56496.4[g]	4.30	*Swift*
LSQ 14mo	0.253	1288	56687[h]	56624[i]	6.59	*Swift*
LSQ 14an	0.163	787	56689[j]	56513[j]	6.13	*Swift*
CSS140925-005854	0.46	2590	56920[k]	56900[k]	3.99	*Swift*
LSQ 14fxj	0.36	1937	56942[l]	56872[m]	3.28	*Swift*
DES15S2nr	0.220	1099	57251[n]	57251[o]	3.02	*Swift*
SN 2016ard/PS16aqv	0.2025[p]	988	57438[q]	57393[r]	3.97	*Swift*

Notes.
[a] From Levan et al. (2013).
[b] From Quimby et al. (2011c), the peak time is MJD 55069.145 and the rest-frame rise-time is ∼50 days.
[c] From Quimby et al. (2011c), the peak time is MJD 55279 and the rest-frame rise-time is ∼23 days.
[d] Vinko et al. (2012) report that SN 2010kd reached maximum light 40 days after discovery. We assume a 50 day rest-frame rise-time.
[e] From Inserra et al. (2013).
[f] From Yan et al. (2015).
[g] Yan et al. (2015) report a range of explosion dates between MJD 56470.8 and MJD 56522.0. We use the middle date MJD 56496.4.
[h] From Leloudas et al. (2015a).
[i] Peak time on MJD 56699 (Leloudas et al. 2015a). The pre-max evolution is only sparsely sampled (see Leloudas et al. 2015a). We assume a 50 day rest-frame rise-time, similar to other SLSNe-I.
[j] From Jerkstrand et al. (2017).
[k] From the CRTS source catalog http://nesssi.cacr.caltech.edu/catalina/AllSN.arch.html
[l] From Smith et al. (2014).
[m] According to Smith et al. (2014), on 2014 Nov 22 the transient was 4–5 weeks rest-frame after maximum light. The inferred time of maximum light is MJD 56940. We assume a 50 days rest-frame rise-time.
[n] From D'Andrea et al. (2015).
[o] Very sparse photometric coverage. On MJD 57286 D'Andrea et al. (2015) reported that the transient is still before the peak. We adopt the discovery date as a rough proxy for the explosion date here.
[p] From P. Blanchard et al. (2018, in preparation).
[q] From http://star.pst.qub.ac.uk/ps1threepi/psdb/public/.
[r] The peak time is MJD 57453 from http://star.pst.qub.ac.uk/ps1threepi/psdb/public/. We assume a 50 day rest-frame rise-time.

X-ray coverage (Table 2), while the "iron sample" comprises 10 SLSNe-I with very sparse optical and X-ray data (Table 3). Given the peculiar nature of ASASSN-15lh (Dai et al. 2015; Metzger et al. 2015; Bersten et al. 2016; Chatzopoulos et al. 2016; Dong et al. 2016; Godoy-Rivera et al. 2017; Kozyreva et al. 2016; Leloudas et al. 2016; Sukhbold & Woosley 2016; van Putten & Della Valle 2017; Margutti et al. 2017a), this transient is not part of the sample of bona fide SLSNe-I analyzed here. However, we discuss and compare the X-ray properties of ASASSN-15lh in the context of SLSNe-I in Section 4, 5.1 and 5.2.

Swift-XRT data have been analyzed using HEASOFT (v6.18) and corresponding calibration files, following standard procedures (see Margutti et al. 2013b for details). For each SLSN-I we provide stacked flux limits (for visualization purposes only), and flux limits derived from individual observations (see Table 5 in the Appendix). *CXO* data have been analyzed with the CIAO software package (v4.9) and corresponding calibration files. Standard ACIS data filtering has been applied. *XMM* data have been analyzed with SAS (v15.0). For the non-detections, we perform a flux calibration adopting a power-law spectral model with index $\Gamma = 2$ corrected for the Galactic neutral-hydrogen absorption along the line of sight (Tables 1–3), as inferred from Kalberla et al. (2005). The details of the X-ray observations of specific SLSNe-I are provided in Section 2.1 for the gold sample, and in the Appendix for all the other SLSNe-I. Data tables can also be found in the Appendix. Figure 1 shows the complete sample of X-ray observations of SLSNe-I.

2.1. Gold Sample

There are four objects in the gold sample: SCP 06F6, PTF 12dam, PS1-14bj, and SN 2015bn (Table 1). In this section we describe the discovery and properties of each object in the gold sample.

2.1.1. SCP 06F6

X-ray emission at the location of the type-I SLSN SCP 06F6 was first reported by Gänsicke et al. (2009) from *XMM* observations obtained 162 days after the initial detection of SCP 06F6 (PI Shartel, ID 0410580301). Levan et al. (2013) derived an X-ray flux $F_x \sim 10^{-13}$ erg s^{-1} cm^{-2} (0.3–10 keV) on 2006 August 2 (MJD 53949, ∼80 days rest-frame since explosion). Given the importance of the claim, we independently reanalyzed the *XMM* observations of SCP 06F6. We confirm the presence of severe contamination by soft proton flares and we confirm the detection of a point-like X-ray source

Table 3
Iron Sample

SN	z	d_L (Mpc)	Discovery Date (MJD)	Inferred Explosion Date (MJD)	NH_{MW} (10^{20} cm^{-2})	Instrument
SN 2009jh/PTF 09cwl	0.349	1868	55010[a]	55010[b]	1.49	*Swift*
PTF 09atu	0.501	2870	55016[a]	54988[c]	3.79	*Swift*
PTF 10aagc	0.207	1027	Unclear	55413[d]	2.61	*Swift*
SN 2010md/PTF 10hgi	0.098	463	55331[a]	55323[e]	5.81	*Swift*
PS1-11bdn	0.738	4601	55910.4[f]	55889.2[f]	3.76	*Swift*
PTF 11rks	0.19	933	55916[a]	55912[e]	4.66	*Swift*
DES15C3hav	0.392	2142	57310[g]	57270[h]	0.705	*Swift*
OGLE15qz	0.63	3790	57264	57264[i]	4.28	*Swift*
OGLE15sd	0.656	3319	57295	57295[i]	9.44	*Swift*
PS16op	0.48	2726	57398[j]	57323[k]	6.73	*Swift*

Notes.
[a] From Levan et al. (2013).
[b] The time of the peak is MJD 55081 and the rise-time is ∼50 days in the rest-frame (Quimby et al. 2011c).
[c] The time of maximum light is MJD 55063 (Quimby et al. 2011c). We assume a 50 day rise-time in the rest-frame.
[d] The time of maximum light is MJD 55473 (Perley et al. 2016). We assume a 50 day rise-time in the rest-frame.
[e] From Inserra et al. (2013).
[f] From R. Lunnan et al. (2018, in preparation).
[g] From Challis et al. (2016).
[h] From Challis et al. (2016) the peak time is MJD 57340. We assume a 50 day rest-frame rise-time.
[i] From http://ogle.astrouw.edu.pl/ogle4/transients/transients.html.
[j] From Dimitriadis et al. (2016).
[k] The peak time is MJD 57397 (Dimitriadis et al. 2016). We assume a 50 day rest-frame rise-time.

in the 0.2–2 keV energy range in MOS1 and MOS2. The source is detected at the $\sim 5\sigma$ confidence level at coordinates R.A. $= 14^{h}32^{m}27^{s}.586$, decl. $= 33°32'25''.33$ (J2000), consistent within the $4''$ position error with the optical position of SCP 06F6. The 0.3–10 keV flux inferred from the count rate $(12.8 \pm 2.3) \times 10^{-3}$ cts s^{-1} is in agreement with the findings from Levan et al. (2013).

Follow-up observations of SCP 06F6 with the *CXO* obtained on 2006 November 4 (MJD 54043, ∼126 days rest-frame since explosion, PI Murray, ID 7010) led to a non-detection. The corresponding flux limit is $F_x < 1.4 \times 10^{-14}$ erg s^{-1} cm^{-2} (Levan et al. 2013). We adopt these flux values here and the correct redshift for this event, which is $z = 1.189$ (Quimby et al. 2011c).

2.1.2. X-Ray Emission at the Location of PTF 12dam

PTF 12dam (Nicholl et al. 2013; Chen et al. 2015; Inserra et al. 2017; Vreeswijk et al. 2017) belongs to the small subset of SLSNe-I with slowly evolving optical light curves. At the time of writing, this group includes SN 2007bi, PTF 12dam, iPTF 13ehe, SN 2015bn, PS1-14bj, and LSQ 14an. The slow evolution of these transients, and of SN 2007bi in particular, inspired a connection with pair-instability explosions (Gal-Yam et al. 2009) that was later debated by Nicholl et al. (2013). X-ray observations of the SLSN-I PTF 12dam have been obtained with *Swift*-XRT and the *CXO*. *Swift*-XRT observations span the time range of ∼43–900 days rest-frame since explosion and revealed no detection down to a flux limit $F_x \sim 5 \times 10^{-14}$ erg s^{-1} cm^{-2} (Figure 2, Table 5).

A set of three deep *CXO* observations was acquired between 2012 June 11 and 19 ($\delta t \sim 60$–68 days rest-frame since explosion; observations IDs 13772, 14444 and 14446, PI Pooley). An X-ray source with a soft spectrum is clearly detected in the merged event file (total exposure of 99.9 ks) at the location of PTF 12dam with significance of 4.8σ in the 0.5–2 keV energy range. The measured net count rate is $(7.1 \pm 2.8) \times 10^{-5}$ c s^{-1} (0.5–2 keV), which corresponds to an unabsorbed flux of $(7.3 \pm 2.9) \times 10^{-16}$ erg s^{-1} cm^{-2} (0.3–10 keV) assuming a power-law spectrum with photon index $\Gamma = 2$. For a thermal bremsstrahlung spectrum with $T = 0.24$ keV (see below) the corresponding unabsorbed flux is $(8.9 \pm 3.5) \times 10^{-16}$ erg s^{-1} cm^{-2} (0.3–10 keV), and $(3.5 \pm 1.4) \times 10^{-16}$ erg s^{-1} cm^{-2} (0.5–2 keV). In both cases, the inferred X-ray luminosity is $L_x \sim 2 \times 10^{40}$ erg s^{-1} in the 0.3–10 keV (Figure 2).

PTF 12dam exploded in a compact dwarf galaxy with fairly large star formation rate SFR $\sim 5\ M_\odot$ yr^{-1} (Lunnan et al. 2014; Chen et al. 2015; Leloudas et al. 2015b; Thöne et al. 2015; Perley et al. 2016) Following Mineo et al. (2012), the expected apparent diffuse X-ray emission associated with star formation is $L_x/\mathrm{SFR} \approx 8.3 \times 10^{38}$ erg s^{-1}($M_\odot$ yr^{-1})$^{-1}$, which translates into $L_x \approx 4.2 \times 10^{39}$ erg s^{-1} (0.5–2 keV) for SFR $\sim 5\ M_\odot$ yr^{-1}. As a comparison, for a thermal bremsstrahlung spectrum with $T = 0.24$ keV (average temperature of the unresolved X-ray component in galaxies, Mineo et al. 2012), for PTF 12dam we calculate $L_x \approx (1.0 \pm 0.4) \times 10^{40}$ erg s^{-1} (0.5–2 keV). We therefore conclude that star formation in the host galaxy of PTF 12dam is likely contributing to at least some of the X-ray luminosity that we detected at the location of the transient. In the following analysis sections we treat our measurements as upper limits to the X-ray emission from PTF 12dam. These observations provide the deepest limits to the X-ray emission from a SLSN-I to date. Future observations will constrain the late-time behavior of the X-ray emission at the location of PTF 12dam and will clarify its association to the optical transient.

2.1.3. PS1-14bj

Two epochs of deep X-ray observations of the type-I SLSN PS1-14bj (Lunnan et al. 2016) have been obtained with *XMM*

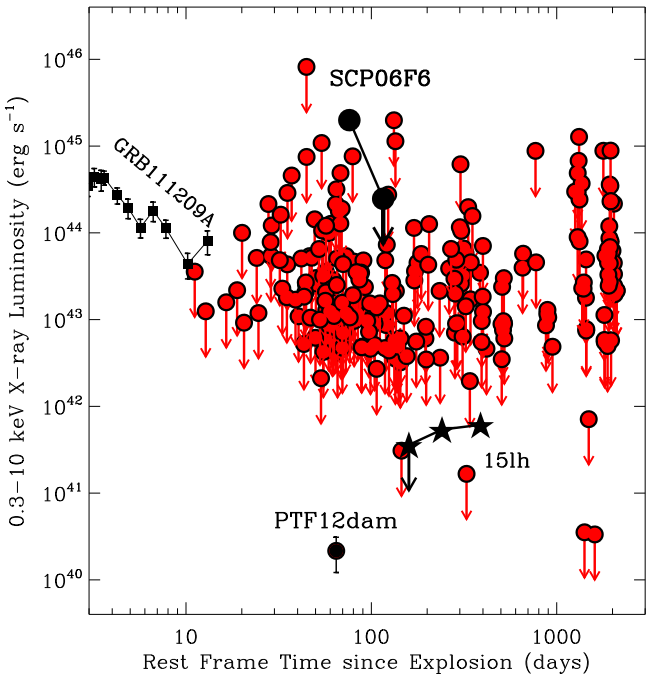

Figure 1. X-ray observations of SLSNe-I spanning the time range ∼10–2000 days (red circles for upper limits, black circles for detections) show that superluminous X-ray emission of the kind detected at the location of SCP 06F6 (Gänsicke et al. 2009; Levan et al. 2013) is not common. Black stars: X-ray emission at the location of ASASSN-15lh (Margutti et al. 2017b), which has a very disputed physical origin. Black squares: X-ray afterglow of GRB 112109A, associated with the overluminous SN 2011kl (Greiner et al. 2015).

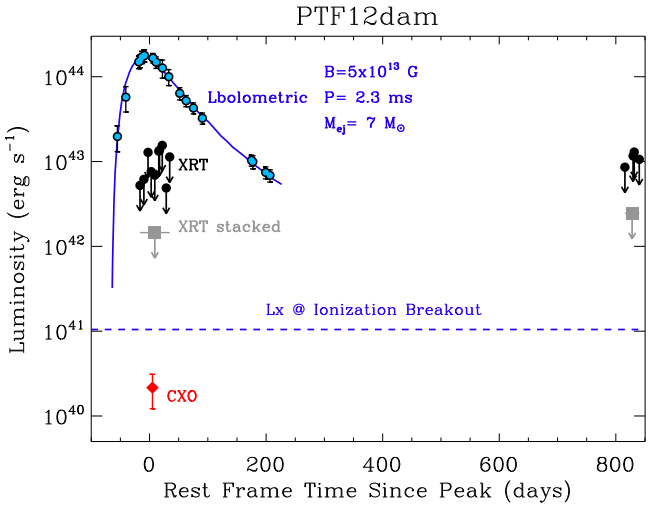

Figure 2. Deep *CXO* observations (red diamond) obtained around the time of the optical peak reveal the presence of soft X-ray emission at the location of PTF 12dam, with luminosity $L_x \sim 2 \times 10^{40}$ erg s^{-1}. Black filled circles: X-ray luminosity limits from *Swift*-XRT. Gray filled squares: stacked limits from *Swift*-XRT observations. Blue filled circles: bolometric optical emission as computed by Nicholl et al. (2013). Blue solid line: best-fitting magnetar model from Nicholl et al. (2013) with parameters reported in Table 4. Horizontal blue dashed line: X-ray luminosity at the time of ionization breakout according to the equations in Section 5.2 for the best-fitting magnetar parameters (Table 4). The expected time of ionization breakout is $t_{\rm ion} = 4.7$ yr; see Table 4.

(PI Margutti, IDs 0743110301, 0743110701) on 2014 June 9 ($\delta t \sim 135$ days rest-frame since explosion, exposure time of 47.6 ks), and 2014 November 7 ($\delta t \sim 235$ days rest-frame

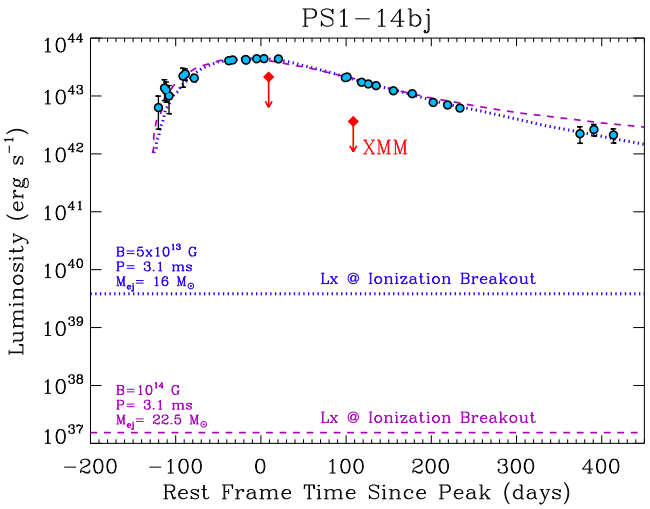

Figure 3. Luminosity limits on the X-ray emission from PS1-14bj obtained with *XMM* (red diamonds). Blue filled circles: bolometric luminosity as computed by Lunnan et al. (2016). Blue dotted line and purple dashed line: magnetar models that adequately fit the observations as computed by Lunnan et al. (2016; see Table 4). Horizontal lines: X-ray luminosity at the time of ionization breakout according to the equations in Section 5.2 for the two magnetar models. For these models, the expected time of ionization breakout is $t_{\rm ion} \geqslant 25$ years; see Table 4.

since explosion, exposure of 36.0 ks). The net exposure times after removing data with high background contamination are 3.6 ks and 29.8 ks, respectively (EPIC-pn data). We do not find evidence for significant X-ray emission at the location of PS1-14bj in either observation and derive a 3σ 0.3–10 keV count-rate upper limit of 9.4×10^{-3} c s^{-1} (1.5×10^{-3} c s^{-1}) for the first (second) epoch, which translates into an unabsorbed flux of 1.9×10^{-14} erg s^{-1} cm^{-2} (3.3×10^{-15} erg s^{-1} cm^{-2}). The corresponding luminosity limits are shown in Figure 3 and reported in Table 5. Analogous with the type of analysis performed on SCP 06F6, we also inspected the 0.2–2 keV images (for both EPIC-pn and MOS) without filtering for the flares. However, for PS1-14bj we confirm the non-detection in both epochs.

2.1.4. SN 2015bn

X-ray observations of the SLSN-I 2015bn (Nicholl et al. 2016a, 2016b) have been obtained with *Swift*-XRT and *XMM* (PI Margutti, IDs 0770380201, 0770380401). A first set of observations was presented in Nicholl et al. (2016a), while Inserra et al. (2017) included in their analysis five *Swift*-XRT pointings. Here, we present the complete data set. *Swift*-XRT started observing SN 2015bn on 2015 February 19 until 2016 July 23, covering the time period ∼44–522 days since explosion rest-frame. No statistically significant X-ray emission is blindly detected at the location of the transient (Figure 4).[13]

[13] We note the presence of marginally significant (2σ c.l.) soft X-ray emission (i.e., <0.3 keV) with $L_x \sim 5 \times 10^{42}$ erg s^{-1} found in a targeted search of data acquired on 2015 February 22 (i.e., ∼55 days since explosion, rest-frame). However, emission with this flux is ruled out by *Swift*-XRT observations obtained 24 hr before, and is not detected in *Swift*-XRT data with similar exposure time collected in the days afterward. Furthermore, we find no evidence for X-ray emission when we filter the event file in the standard 0.3–10 keV energy range, which is where the *Swift*-XRT is properly calibrated. We conclude that the association of the targeted detection with real X-ray emission from SLSN-I 2015bn/PS15ae is highly questionable and therefore proceed with the conclusion that there is no statistically significant X-ray emission at the location of the transient.

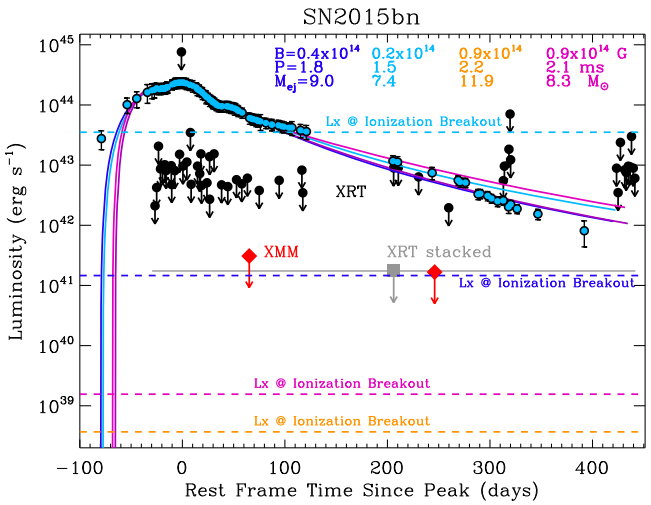

Figure 4. Results from our joint *Swift*-XRT and *XMM* X-ray campaign (black filled circles, gray squares and red diamonds) in the context of the optical bolometric luminosity of SN 2015bn and the best-fitting magnetar models as derived by Nicholl et al. (2016b; see Table 4). Horizontal dashed lines: expected X-ray luminosity at the time of the ionization breakout, which is $t_{\rm ion} = 5$ yr (for $B = 0.4 \times 10^{14}$ G, $P = 1.8$ ms, $M_{\rm ej} = 9\,M_\odot$), $t_{\rm ion} = 0.6$ yr (for $B = 0.2 \times 10^{14}$ G, $P = 1.5$ ms, $M_{\rm ej} = 7.4\,M_\odot$), $t_{\rm ion} = 45$ yr (for $B = 0.9 \times 10^{14}$ G, $P = 2.2$ ms, $M_{\rm ej} = 11.9\,M_\odot$), $t_{\rm ion} = 22$ yr (for $B = 0.9 \times 10^{14}$ G, $P = 2.1$ ms, $M_{\rm ej} = 8.3\,M_\odot$) as reported in Table 4. The models with the shortest spin periods are disfavored by our X-ray limits. This figure clearly shows how magnetar models associated with very similar bolometric optical light curves do predict instead very different X-ray luminosities at ionization breakout. The X-ray luminosity at the time of breakout is a very sensitive probe of the properties of central engines in SLSNe.

Two epochs of *XMM* observations have been obtained on 2015 June 1 ($\delta t \sim 145$ days rest-frame since explosion) and 2015 December 18 ($\delta t \sim 325$ days rest-frame since explosion) with exposure times of 28.0 ks and 25.1 ks, respectively (EPIC-pn data). After excluding time intervals heavily affected by proton flaring, the net exposure times are 7.3 and 18.8 ks. No X-ray source is detected at the location of the SLSN-I 2015bn. We derive a 3σ 0.3–10 keV count-rate upper limit of 4.2×10^{-3} c s^{-1} (2.3×10^{-3} c s^{-1}) for the first (second) epoch, which translates into an unabsorbed flux of 9.8×10^{-15} erg s^{-1} cm^{-2} (5.3×10^{-15} erg s^{-1} cm^{-2}). The results from our X-ray campaign are listed in Table 5 and displayed in Figure 4.

3. Search for Superluminous X-Ray Emission in SLSNe-I

In this section we derive constraints on the possible presence of superluminous X-ray emission in SLSNe-I that was not detected because of the discontinuous observational coverage. No assumption is made about the physical nature of the emission. SLSNe-I are treated here as different realizations of the same stochastic process (which is the underlying assumption behind any sample analysis).

The hypothesis we test is that superluminous X-ray emission of the kind detected at the location of SCP 06F6 (i.e., isotropic $L_x \sim 10^{45}$ erg s^{-1}) is ubiquitous in SLSNe-I. We furthermore assume that the superluminous X-ray emission is "on" for a total time $\Delta t_{\rm active}$ (not necessarily continuous) and shuts on and off instantaneously, and that the probability of turning on is uniformly distributed during the interval of time of investigation. Our sample of observations comprises 253 spacecraft pointings, for a total observing time of ~30 days at $t < 2000$ days (rest-frame). Out of 253 trials, observations only led to one success (i.e., in the case of SCP 06F6). We can use simple binomial probability arguments to constrain the maximum and minimum $\Delta t_{\rm active}$ that would be statistically consistent at the 3σ c.l. with $\leqslant 1$ successes (for $\Delta t_{\rm active,max}$) and $\geqslant 1$ successes (for $\Delta t_{\rm active,min}$) out of N trials, where $N \equiv N(t)$. In this context a trial consists of an observation that is deep enough to be sensitive to $L_x \sim 10^{45}$ erg s^{-1}. For each trial, the probability of success is $p = \Delta t_{\rm active}/\Delta t_{\rm total}$, where $\Delta t_{\rm total}$ is the entire range of times during which we conduct our search for superluminous X-ray emission (for the entire sample, $\Delta t_{\rm total} \sim 2000$ days). For $t < 100$ days, $\Delta t_{\rm total} \sim 90$ days (i.e., our search starts at $t \sim 10$ days), $N = 110$. With these parameters we find 200 s $\leqslant \Delta t_{\rm active} \leqslant 5 \times 10^5$ s. For shorter $\Delta t_{\rm active}$ the probability of having one success out of N trials is below the 3σ c.l., while for longer $\Delta t_{\rm active}$ we would have expected to have more successes in our search at 3σ c.l. If we consider the entire sample of observations $\Delta t_{\rm total} \sim 2000$ days, $N = 253$ and we find 2000 s $\leqslant \Delta t_{\rm active} \leqslant 5 \times 10^6$ s. As a cross-check, under the same assumptions, but adopting the Bayesian technique of Romano et al. (2014) we obtain for $\Delta t_{\rm active}$ similar upper limits.

We conclude that superluminous X-ray emission is not a common trait of SLSNe-I. *If* present, the superluminous X-ray emission requires peculiar physical circumstances to manifest and its duration is $\leqslant$2 months at $t < 2000$ days and $\leqslant$ few days at $t < 100$ days.

4. Constraints on SLSNe-I Environments

Inverse Compton (IC) emission is a well-known source of X-rays in young stellar explosions (Björnsson & Fransson 2004; Chevalier & Fransson 2006). X-ray emission originates from the up-scattering of optical photons from the SN photosphere by a population of relativistic electrons accelerated at the shock front. While always present, IC is the dominant emission mechanism at early times ($t \leqslant$ optical peak) for SNe propagating into low-density media. In the case of strong SN shock interaction with the medium, the dominant X-ray emission mechanism is instead bremsstrahlung (Björnsson & Fransson 2004; Chevalier & Fransson 2006), as it is indeed observed in type-IIn SNe and as recently confirmed by the first broadband X-ray spectra of strongly interacting SNe (Ofek et al. 2014; Margutti et al. 2017a). The analysis of the optical emission from SLSNe-I in the context of the interaction model (e.g., Nicholl et al. 2014, 2016b) suggests that *if* SLSNe-I are powered by interaction, then the shock breaks out around the time of optical maximum light and the medium consists of a thick shell confined to small radii ($R \sim 5 \times 10^{15}$ cm for SN 2015bn) surrounded by a lower density region. This conclusion is consistent with the lack of observed narrow lines in the optical spectra of SLSNe-I (in sharp contrast to ordinary and superluminous type-IIn SNe): the presence of an extended unshocked region of dense circumstellar medium (CSM) would likely imprint low-velocity features that are *not* observed in SLSNe-I (see also Chevalier & Irwin 2011). The X-ray observations that we will use in this section have been obtained at the time of maximum light or later, which is after the shock has broken out from the thick shell of material *if* a shell is there. In the following, we thus constrain the density around SLSNe-I under the conservative assumption that IC is the *only* source of X-ray radiation. Since we sample the time range $t > t_{\rm peak}$, our density limits apply to the region $R \gtrsim 10^{16}$ cm.

Table 4
Magnetar Parameters (Magnetic Field B, Spin Period P_i, and Ejecta Mass M_{ej}), Estimated from the Bolometric Optical Emission, and Corresponding Ionization Breakout Times t_{ion} and X-Ray Luminosities $L_x(t_{ion})$

SN	B (G)	P_i (ms)	M_{ej} ($M_\odot$)	References	t_{ion} (years)	$L_x(t_{ion})$ (erg s^{-1})
SN 2010md/PTF 10hgi	3.6×10^{14}	7.2	3.9	Inserra et al. (2013)	76.3	7.8×10^{36}
SN 2010gx	7.4×10^{14}	2.0	7.1	Inserra et al. (2013)	1070	9.4×10^{33}
PTF 11rks	6.8×10^{14}	7.50	2.8	Inserra et al. (2013)	140	6.5×10^{35}
SN 2011ke	6.4×10^{14}	1.7	8.6	Inserra et al. (2013)	1170	1.0×10^{34}
PTF 12dam	5×10^{13}	2.3	7	Nicholl et al. (2013)	4.7	1.0×10^{41}
SN 2012il	4.1×10^{14}	6.1	2.3	Inserra et al. (2013)	34.5	3.0×10^{37}
iPTF 13ehe	8×10^{13}	2.55	35	Wang et al. (2016a)	304	1.0×10^{37}
PS1-14bj	10^{14}	3.1	22.5	Lunnan et al. (2016)	196	1.5×10^{37}
	5×10^{13}	3.1	16	Lunnan et al. (2016) w. leakage	24.8	3.8×10^{39}
SN 2015bn/PS15ae	0.9×10^{14}	2.1	8.4	Nicholl et al. (2016b)	22.1	1.5×10^{39}
	10^{14}	1.7	15.1	Nicholl et al. (2016b)	88.4	7.6×10^{37}
	0.9×10^{14}	2.1	8.3	Nicholl et al. (2016a)	21.6	1.6×10^{39}
	0.2×10^{14}	1.5	7.4	Nicholl et al. (2016a)	0.64	3.5×10^{43}
	0.9×10^{14}	2.2	11.9	Nicholl et al. (2016a)	44.5	3.7×10^{38}
	0.4×10^{14}	1.8	9.0	Nicholl et al. (2016a)	5.02	1.5×10^{41}

The X-ray emission from IC depends on (i) the density structure of the SN ejecta and of the CSM, (ii) the details of the electron distribution responsible for the up-scattering, (iii) the explosion parameters (ejecta mass M_{ej} and kinetic energy E_k), and (iv) the availability of seed optical photons ($L_{x,IC} \propto L_{bol}$, where L_{bol} is the bolometric optical luminosity). We employ the formalism of Margutti et al. (2012) modified to reflect the stellar structure of massive stars as in Margutti et al. (2014). We further assume a wind-like medium with $\rho_{CSM} \propto R^{-2}$ as appropriate for massive stars, a power-law electron distribution $n_e(\gamma) = n_0 \gamma^{-p}$ with $p \sim 3$ as indicated by radio observations of H-stripped core-collapse SNe (Chevalier & Fransson 2006) and a fraction of post-shock energy into relativistic electrons $\epsilon_e = 0.1$ (e.g., Chevalier & Fransson 2006). Since $L_{x,IC} \propto L_{bol}$, it is clear that the tightest constraints on ρ_{CSM} will be derived from the most nearby SLSNe-I, which have very bright optical emission and deep X-ray limits (i.e., they have the largest flux ratio F_{opt}/F_x constrained by observations). To this end, we analyze below the SLSNe-I 2015bn and PTF 12dam. We also provide constraints for the peculiar transient ASASSN-15lh.

For SN 2015bn we follow Nicholl et al. (2016a) and Nicholl et al. (2016b) and adopt a range of ejecta masses $M_{ej} = 7$–$15\ M_\odot$ (Table 4). With these parameters and the optical bolometric light curve from Nicholl et al. (2016b; Figure 4), our X-ray non-detections constrain the pre-explosion mass-loss rate from the stellar progenitor of SN 2015bn to $\dot{M} < 10^{-2}\ M_\odot\ \mathrm{yr}^{-1}$ ($\dot{M} < 10^{-1}\ M_\odot\ \mathrm{yr}^{-1}$) for $E_k = 10^{52}$ erg ($E_k = 10^{51}$ erg) and wind velocity $v_w = 1000\ \mathrm{km\ s}^{-1}$, (Figures 5, 6), which is $\dot{M} < 10^{-4}\ M_\odot\ \mathrm{yr}^{-1}$ ($\dot{M} < 10^{-3}\ M_\odot\ \mathrm{yr}^{-1}$) for wind velocity $v_w = 10\ \mathrm{km\ s}^{-1}$. In this context, the analysis of the radio observations of SN 2015bn indicates $\dot{M} < 10^{-2}\ M_\odot\ \mathrm{yr}^{-1}$ for $v_w = 10\ \mathrm{km\ s}^{-1}$ at $R > 10^{15}$ cm, while $\dot{M} \sim 10^{-2}\ M_\odot\ \mathrm{yr}^{-1}$ would be needed to explain the late-time optical light curve of the transient through continued ejecta-CSM interaction (Nicholl et al. 2016b). The X-ray analysis thus argues against the presence of an extended CSM region if $E_k > 10^{51}$ erg (as is likely the case) and suggests that another source of energy is powering the light curve after the peak. This result is consistent with the conclusions by Nicholl et al. (2016a): based on the spectroscopic similarity of SN 2015bn with the GRB SN 1998bw in the nebular phase, Nicholl et al. (2016a) concluded that a central engine is driving the explosion.

For PTF 12dam we use $M_{ej} = 7\ M_\odot$, as inferred by Nicholl et al. (2013) from the modeling of the optical bolometric emission (Table 4). We detect an X-ray source at the location of PTF 12dam with $L_x \sim 2 \times 10^{40}$ erg s^{-1}. We treat this value as an upper limit to the X-ray luminosity from the transient to account for possible contamination from the host galaxy. For these values of the explosion parameters and the measured L_x, the inferred mass-loss rate is $\dot{M} < 2 \times 10^{-5}\ M_\odot\ \mathrm{yr}^{-1}$ ($\dot{M} < 4 \times 10^{-6}\ M_\odot\ \mathrm{yr}^{-1}$) for $E_k = 10^{51}$ erg ($E_k = 10^{52}$ erg) and $v_w = 1000\ \mathrm{km\ s}^{-1}$ (Figures 5, 6). These are the tightest constraints to the pre-explosion mass-loss history of SLSNe-I progenitors.

If the peculiar transient ASASSN-15lh is associated with an $E_k = 10^{52}$ erg explosion with ejecta mass $M_{ej} = 5$–$10\ M_\odot$ (Metzger et al. 2015; Bersten et al. 2016; Chatzopoulos et al. 2016; Dai et al. 2016; Dong et al. 2016; Kozyreva et al. 2016; Sukhbold & Woosley 2016), the X-ray observations from Margutti et al. (2017b) imply $\dot{M} < 5 \times 10^{-6}\ M_\odot\ \mathrm{yr}^{-1}$ ($\dot{M} < 5 \times 10^{-5}\ M_\odot\ \mathrm{yr}^{-1}$) for $v_w = 1000\ \mathrm{km\ s}^{-1}$ for a thermal (non-thermal) X-ray spectrum. These values are typical of mass-loss rates from H-stripped compact massive stars (Figures 5 and 6).

From our analysis, we conclude that for PTF 12dam the inferred limits rule out the densest environments that characterize type-IIn SNe (Figure 5), indicating that the strong SN shock interaction with an *extended* medium is unlikely to be the primary source of energy sustaining the very luminous display. Our data, however, do not constrain the presence of a dense medium confined to $d < 10^{16}$ cm, which might be the result of massive shell ejections by the stellar progenitor in the $\sim$10 yr before collapse (for a shell ejection velocity of $1000\ \mathrm{km\ s}^{-1}$). Interestingly, a low-density environment with $\dot{M} \sim 4 \times 10^{-6}\ M_\odot\ \mathrm{yr}^{-1}$ was also inferred from radio and X-ray observations of the type-Ib SN 2012au (Kamble et al. 2014), which showed spectroscopic similarities with SLSN-I (Milisavljevic et al. 2013). The tight constraints obtained for PTF 12dam point to a clean environment, and argue against the dense CSM typical of extended progenitors like RSG stars. This result suggests that at least some SLSN-I progenitors are

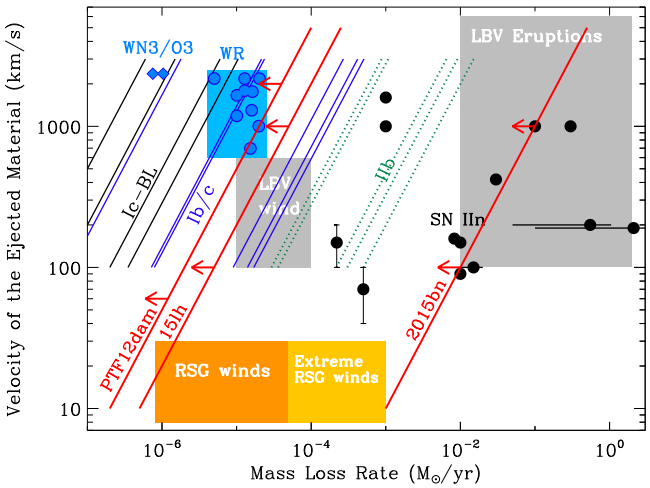

Figure 5. Velocity of the ejected material during mass loss vs. pre-explosion mass-loss rate for H-poor core-collapse SNe (diagonal lines) and type-IIn SNe (black dots). H-poor SNe are represented with diagonal lines since radio and X-ray observations constrain the density $\rho_{\rm CSM}$, which is $\propto \dot{M}/v_w$. The black, blue, and dotted green lines mark the sample of type Ic-BL, Ib/c, and IIb SNe from Drout et al. (2016). SLSNe-I and the transient ASASSN-15lh are in red. For SLSNe-I we conservatively plot the constraints for $E_k = 10^{51}$ erg, which is a *lower limit* to the total kinetic energy of the blast wave (even in the case of a magnetar central engine). The properties of galactic WR stars are from Crowther (2007), while WN3/O3 stars are from Massey et al. (2015). The locations of red supergiant environments (RSG) are from de Jager et al. (1988), Marshall et al. (2004) and van Loon et al. (2005). The typical locations of luminous blue variable (LBV) winds and eruptions are from Smith (2014) and Smith & Owocki (2006). The densest environments that characterize LBV eruptions and type-IIn SNe are not consistent with our deepest SLSNe-I limits. Our tightest constraints on PTF 12dam rule out RSG winds and put PTF 12dam in the same region of the parameter space as H-stripped SNe with broad spectral features (i.e., Ic-BL).

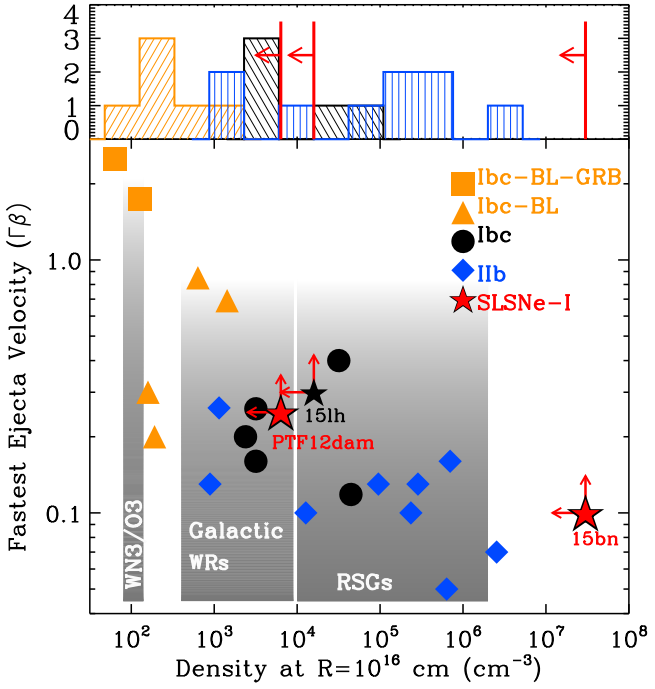

Figure 6. Constraints on the fastest SN ejecta velocity and environmental density of SLSNe-I with the most sensitive X-ray limits (red stars) and the peculiar transient ASASSN-15lh (black star) in the context of core-collapse stellar explosions from H-stripped progenitors. Gray shaded regions: density in the environments of red supergiant stars (RSGs), Wolf–Rayet stars (WRs), and the recently discovered new type of WR stars, WN3/O3 (de Jager et al. 1988; Marshall et al. 2004; van Loon et al. 2005; Crowther 2007; Massey et al. 2015). Type IIb SNe (blue diamonds) explode in the densest environments, while SNe with broad spectroscopic features (orange squares and triangles) are associated with the lowest-density media. For SLSNe-I we conservatively plot the constraints for $E_k = 10^{51}$ erg, which is a *lower limit* to the total kinetic energy of the blast wave (even in the case of a magnetar central engine). In the case of PTF 12dam, our measurements rule out the dense environments associated with RSG winds and are consistent with the clean environments that characterize WRs, WN3/O3, and engine-driven SN explosions. References: van Dyk et al. (1994), Fransson & Björnsson (1998), Berger et al. (2002), Weiler et al. (2002), Ryder et al. (2004), Soderberg et al. (2005, 2006a, 2006b, 2008, 2010a, 2010b), Chevalier & Fransson (2006), Roming et al. (2009), Krauss et al. (2012), Milisavljevic et al. (2013), Corsi et al. (2014), Kamble et al. (2014, 2016), Margutti et al. (2014, 2017a), Chakraborti et al. (2015), Drout et al. (2016).

likely to be compact stars surrounded by a low-density medium at $d > 10^{16}$ cm at the time of stellar death.

5. Central Engines in SLSNe-I

5.1. Constraints on On-axis and Off-axis Collimated and Non-collimated Relativistic Outflows

The search for off-axis and on-axis relativistic GRB-like jets in SLSNe-I is motivated by two recent observational findings: (i) the association of SN 2011kl with GRB 111209A. SN 2011kl bridges the luminosity gap between GRB-SNe and SLSNe-I, and shows similarities to SLSNe-I (Greiner et al. 2015); and (ii) nebular spectroscopy of the SLSN-I 2015bn revealed close similarities to the engine-driven SN 1998bw, associated with GRB 980425, suggesting that the core of engine-driven SNe and SLSNe-I share some key physical properties and structure (Nicholl et al. 2016a).

Early-time X-ray observations of SLSNe-I acquired at $t \lesssim 40$ days generally rule out on-axis collimated ultra-relativistic outflows of the type associated with energetic long GRBs (Figure 7, cloud of filled gray squares). We constrain the presence of off-axis relativistic outflows by generating a grid of off-axis GRB X-ray afterglows with the broadband afterglow numerical code Boxfit v2 (van Eerten et al. 2012).[14] The observed X-ray emission depends on the kinetic energy E_k of the outflow, the density of the medium $\rho_{\rm CSM}$ (we explore both an ISM-like medium $n_{\rm CSM} = {\rm const}$ and a wind-like medium with $\rho_{\rm CSM} \propto R^{-2}$), the microphysical shock parameters ϵ_B and ϵ_e (post-shock energy fraction in magnetic field and electrons, respectively), the jet opening angle θ_j and the angle of the jet with respect to the line of sight $\theta_{\rm obs}$. We explore the predicted X-ray signatures of collimated $\theta_j = 5°$ outflows with $\epsilon_e = 0.1$ and $\epsilon_B = 0.01$ (as derived from first-principle simulations of relativistic shocks, e.g., Sironi et al. 2015), isotropic kinetic energy in the range $E_{k,\rm iso} = 10^{52}$–10^{55} erg, environment density in the range $n = 10^{-3}$–$10\ {\rm cm}^{-3}$ (ISM) or mass-loss rate $\dot{M} = 10^{-7}$–$10^{-3}\ M_\odot\ {\rm yr}^{-1}$ (wind) and observed angles $\theta_{\rm obs} \leqslant 90°$. These values are representative of the parameters inferred from accurate modeling of broadband afterglows of GRBs.

Based on these simulations and the X-ray observations from the entire sample of SLSNe-I, we find that relativistic collimated outflows with $E_k > 10^{51}$ erg, $n > 10^{-3}\ {\rm cm}^{-3}$ and $\theta_{\rm obs} < 2\theta_j$ are

[14] http://cosmo.nyu.edu/afterglowlibrary/boxfit2011.html

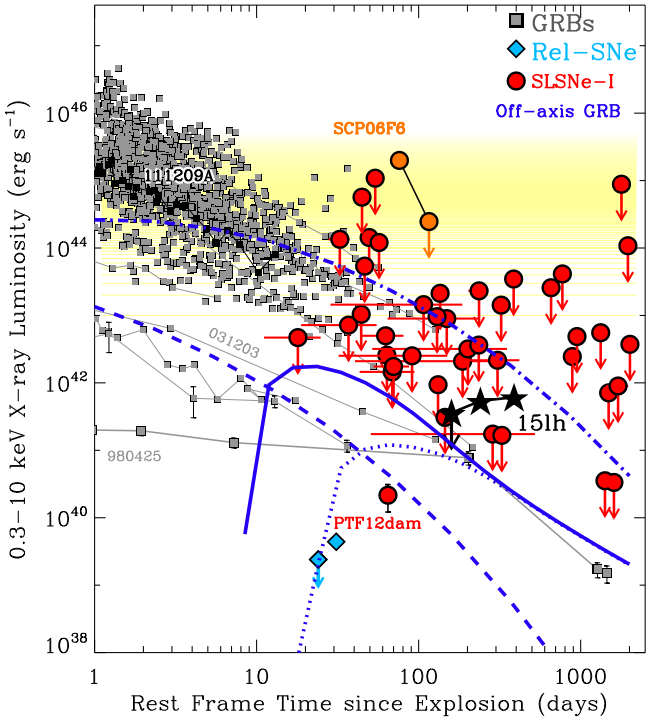

Figure 7. X-ray emission from SLSNe-I (red circles) in the context of detected GRB X-ray afterglows (gray squares, Margutti et al. 2013b), relativistic SNe (blue diamonds, Soderberg et al. 2010b; Margutti et al. 2014) and representative off-axis afterglow models (blue lines) from collimated outflows with $\theta_{\rm jet} = 5°$, $\epsilon_{\rm e} = 0.1$, $\epsilon_{\rm B} = 0.01$, $E_k = 4 \times 10^{52}$ erg, $\dot{M} = 10^{-3}\,M_\odot$ yr^{-1}, $\theta_{\rm obs} = 30°$ (thick line) and $\theta_{\rm obs} = 45°$ (dotted line). We also show models for $\dot{M} = 10^{-7}\,M_\odot$ yr^{-1}, $\theta_{\rm obs} = 2\theta_{\rm jet}$, $E_k = 4 \times 10^{52}$ erg (dotted–dashed line), and $E_k = 4 \times 10^{50}$ erg (dashed line). The fast-fading X-ray emission at the location of SCP 06F6 is shown with orange circles (Levan et al. 2013). Black stars: steady X-ray emission at the location of ASASSN-15lh (Margutti et al. 2017b). Black squares: X-ray afterglow of GRB 111209A, associated with the overluminous SN 2011kl (Greiner et al. 2015). In this plot we show the *Swift*-XRT limits from the stacked analysis for display purposes. The analysis and results are based on the time-resolved observations. Notably, our deepest limits rule out non-collimated outflows from the weakest GRB explosions, like GRB 980425 (Pian et al. 2000; Kouveliotou et al. 2004).

ruled out. Powerful jets with $E_k > 10^{52}$ erg expanding in a thick medium with $n \geqslant 10$ cm^{-3} and $\theta_{\rm obs} \leqslant 30°$ are also ruled out. For a wind environment, our observations are not consistent with jets with $E_k > 10^{50.5}$ erg expanding in a medium enriched with $\dot{M} \geqslant 10^{-7}\,M_\odot$ yr^{-1} and $\theta_{\rm obs} < 2\theta_j$. At higher kinetic energies, observations rule out jets with $E_k > 10^{51.5}$ erg, $\dot{M} \geqslant 10^{-4}\,M_\odot$ yr^{-1}, and $\theta_{\rm obs} \leqslant 30°$ or $E_k > 10^{52}$ erg, $\dot{M} \geqslant 10^{-3}\,M_\odot$ yr^{-1}, and $\theta_{\rm obs} \leqslant 45°$.We are not sensitive to jets viewed at $\theta_{\rm obs} > 30°$ for the ISM, and $\theta_{\rm obs} > 45°$ for the wind medium.

In the case of PTF 12dam, observations argue against jets with $E_k > 10^{51}$ erg propagating into a medium with $n > 10^{-3}$ cm^{-3} or $\dot{M} > 10^{-7}\,M_\odot$ yr^{-1} and $\theta_{\rm obs} < 2\theta_j$. The portion of the parameter space associated with $E_k = 10^{50.5}$ erg, $\dot{M} \sim 10^{-6\text{–}7}\,M_\odot$ yr^{-1} and $\theta_{\rm obs} < 2\theta_j$ is also ruled out. Dense environments with $n > 10$ cm^{-3} or $\dot{M} > 10^{-4}\,M_\odot$ yr^{-1} would also produce X-ray emission in excess of what we observed for outflows with $E_k > 10^{51}$ erg viewed at $\theta_{\rm obs} < 30°$.

For the SLSN-I 2015bn observations rule out systems with $E_k > 10^{52}$ erg, $n > 10^{-3}$ cm^{-3}, or $\dot{M} > 10^{-7}\,M_\odot$ yr^{-1} for $\theta_{\rm obs} < 2\theta_j$. Even the most energetic outflows in our simulations with $E_k > 10^{52}$ erg would fall below our detection threshold for $\theta_{\rm obs} > 30°$ and the range of densities considered. These observations complement the results from deep radio non-detections of SN 2015bn (Nicholl et al. 2016b), which argue against powerful on-axis or off-axis jets with $E_k = 2 \times 10^{51}$ erg propagating into an ISM-like medium with density $n = 1$ cm^{-3}.[15]

Finally, we consider the observable X-ray signatures of *non-collimated* mildly relativistic outflows. X-ray observations of the majority of SLSNe-I in our sample are not sensitive to the faint X-ray emission of mildly relativistic non-collimated outflows typical of low-energy GRBs like 980425, 031203, 060218, and 100316D (e.g., Pian et al. 2000; Kouveliotou et al. 2004; Watson et al. 2004; Soderberg et al. 2006a; Margutti et al. 2013a). However, our deepest X-ray limits obtained with the *CXO* and *XMM* are sensitive enough to probe the parameter space populated by the weakest GRB-SNe. For the SLSN-I 2015bn, our *XMM* observations probe and rule out luminosities $L_x > 2 \times 10^{41}$ erg s^{-1} at $t \sim$ 100–300 days, which are comparable to the detected X-ray emission of GRBs 980425 and 031203 at a similar epoch, $L_x \sim 10^{41}$ erg s^{-1} (Figure 7). Remarkably, in the case of PTF 12dam, *CXO* observations acquired at the time of optical peak rule out even the faintest non-collimated X-ray emission ever detected from a low-energy GRB (Figure 7), indicating that *if* PTF 12dam is an engine-driven stellar explosion, the jet never successfully broke out from the stellar envelope, in close analogy to the picture recently suggested for the relativistic SNe 2009bb and 2012ap (Margutti et al. 2014 and references therein).

To conclude, the analysis of our deep X-ray limits in the context of GRB afterglow simulations and the recent finding of similarity in the nebular emission from SN 2015bn with engine-driven SNe, suggest that *if* SLSNe-I are jet-driven explosions, then either SLSNe-I are powered by very energetic collimated GRB-like outflows that were pointing far away from our line of sight ($\theta_{\rm obs} > 30°$), or that SLSNe-I harbor failed jets that do not successfully break through the stellar envelope and are associated with weak X-ray emission. Late-time radio observations of SN 2015bn (Nicholl et al. 2016a) argue against the off-axis relativistic jet scenario in the case of energetic jets (see also Coppejans et al. 2018; Margalit et al. 2018). However, the association of the overluminous SN 2011kl with GRB 111209A suggests that some SLSNe-I might harbor relativistic jets. We therefore propose that, in strict analogy to H-stripped core-collapse SNe of ordinary luminosity (e.g., Mazzali et al. 2008; Xu et al. 2008; Lazzati et al. 2012; Margutti et al. 2014), SLSNe-I are also characterized by a continuum of jet strengths and lifetimes of the central engine.

5.2. Constraints on Magnetar Central Engines: The Ionization Breakout

We compute the ionization breakout time and the X-ray luminosity at breakout following Metzger et al. (2014) and Metzger & Piro (2014). We consider a central engine with an UV/X-ray luminosity L that releases an energy $L \times t$ in ionizing radiation on a timescale t. The radiation ionizes its way through the ejecta on a timescale

[15] Note that Nicholl et al. (2016b) assumed an ISM-like medium and larger $\epsilon_B = 0.1$ and $\theta_j = 10°$.

$$t_{\rm ion} \approx \begin{cases} 120\ {\rm days}\ M_3^{3/4} v_9^{-5/4} T_5^{-0.2} \left(\frac{X_A}{0.1}\right)^{1/4} \left(\frac{Lt}{10^{52}\ {\rm erg}}\right)^{-1/4} Z_8^{3/4},\ (\eta_{\rm thr} \ll 1) \\ 110\ {\rm days}\ M_3 v_9^{-3/2} T_5^{-0.4} \left(\frac{X_A}{0.1}\right)^{1/2} \left(\frac{Lt}{10^{52}\ {\rm erg}}\right)^{-1/2} Z_8^{3/2},\ (\eta_{\rm thr} \gg 1), \end{cases} \quad (1)$$

where $M_3 \equiv M_{\rm ej}/(3M_\odot)$, $T_5 = T/10^5$ K is the temperature of electrons in the recombination layer, $v_9 \equiv v/10^9$ cm s^{-1}, X_Z is the mass fraction X_Z of elements with atomic number $Z = 8Z_8$ in the ejecta and

$$\eta_{\rm thr} \approx 0.7 \left(\frac{Lt}{10^{52}\ {\rm erg}}\right)^{-1} M_3 v_9^{-1} \left(\frac{X_A}{0.1}\right) T_5^{-0.8} Z_8^3 \quad (2)$$

is the ratio of absorptive and scattering opacity in the ejecta (Metzger et al. 2014). The spin-down timescale $t_{\rm sd}$ of a magnetar central engine is given by

$$t_{\rm sd} \sim 4.7{\rm d} B_{14}^{-2} P_{\rm ms}^2 \quad (3)$$

and the spin-down luminosity is given by

$$L_{\rm sd} = 5 \times 10^{46} B_{14}^2 P_{\rm ms}^{-4} \left(1 + \frac{t}{t_{\rm sd}}\right)^{-2}\ {\rm erg\ s^{-1}} \approx 1.1 \times 10^{48} B_{14}^{-2} t_{\rm d}^{-2}\ {\rm erg\ s^{-1}} \quad (4)$$

for $t \gg t_{\rm sd}$, $B_{14} \equiv B/10^{14}$ G, $P_{\rm ms} \equiv P/{\rm ms}$, $t_{\rm d} \equiv t/{\rm days}$ and we adopted the vacuum dipole spin-down convention employed by Kasen & Bildsten (2010). For $L = L_{\rm sd}$ and $t \gg t_{\rm sd}$ the ionization timescale of Equation (1) can be written as

$$t_{\rm ion} \approx \begin{cases} 280\ {\rm days}\ M_3 v_9^{-5/3} T_5^{-4/15} \left(\frac{X_A}{0.1}\right)^{1/3} B_{14}^{2/3} Z_8,\ (\eta_{\rm thr} \ll 1) \\ 1273\ {\rm days}\ M_3^2 v_9^{-3} T_5^{-4/5} \left(\frac{X_A}{0.1}\right) B_{14}^2 Z_8^3,\ (\eta_{\rm thr} \gg 1). \end{cases} \quad (5)$$

The X-ray luminosity at ionization breakout is $L_x \approx L_{\rm sd}(t_{\rm ion})/14$. In the following we assume that oxygen ($Z_8 = 1$) dominates the bound-free opacity in the ∼keV X-ray band, we use and electron temperature $T = 10^5$ K, $X_A = 0.1$, velocity of the order of 10^9 cm s^{-1} and we compute the ionization timescale and the X-ray luminosity at breakout and compare to our X-ray limits and measurements.

For SLSNe-I with well-constrained optical bolometric emission, we use the magnetar parameters $M_{\rm ej}$, P, and B that best fit the optical bolometric luminosity to estimate $t_{\rm ion}$ and $L_x(t_{\rm ion})$ (Table 4). From Table 4 and Figures 2–4 it is clear that most of the $L_x(t_{\rm ion})$ are too faint to be detected and that $t_{\rm ion}$ is usually much larger than the ∼2000 days that we cover with our observations. However, it is also clear that $t_{\rm ion}$ and $L_x(t_{\rm ion})$ are very sensitive to the magnetar parameters and qualify as excellent probes of central engines in SLSNe-I. Magnetar central engines that would produce very similar optical bolometric outputs that cannot be distinguished with current optical-UV photometry are instead clearly differentiated in their $L_x(t_{\rm ion}) - t_{\rm ion}$ properties. As an example, for the best-fitting magnetar parameters of SN 2015bn in Figure 4, $L_x(t_{\rm ion})$ spans ∼5 orders of magnitude and $t_{\rm ion}$ ranges from 0.6 to 88 years. For this SLSN-I, our deep X-ray limits obtained with *XMM* and the combined limit from *Swift*-XRT favor models with $P > 2$ ms. The fastest spinning magnetar model with $P = 1.5$ ms and relatively small ejecta mass $M_{\rm ej} = 7.4\,M_\odot$ from Nicholl et al. (2016a) predicts $L_x(t_{\rm ion}) > 10^{43}$ erg s^{-1} at $t_{\rm ion} \sim 0.6$ years and it is therefore disfavored by our X-ray observations (Figure 4).

Figure 8 shows how the X-ray observations from our sample compare to the predictions from the magnetar ionization breakout model. We investigate a wide range of central engine parameters $P = 1$–7 ms and $B_{14} = 0.2$–10 G for ejecta masses $M_{\rm ej} = 1$–$20\,M_\odot$. Current X-ray observations are not sensitive to magnetars with $B_{14} \geqslant 2$ (Figure 8). For $B_{14} < 2$, observations favor models with larger ejecta mass: for $B_{14} = 0.2$, 0.5, 1.0 G the allowed parameter space is $M_{\rm ej} > 20$, 7, $3\,M_\odot$. X-ray observations indicate that *if* a magnetar central engine powers the emission from SLSNe-I then it has to be either associated with a large magnetic field or with a large explosion ejecta mass. These results are independent from (but in agreement with) the values inferred from the modeling of the optical emission from SLSNe-I (Table 4, Inserra et al. 2013; Nicholl et al. 2013).

We end by noting that our analytic treatment of ionization breakout from the supernova ejecta requires confirmation by a more detailed photoionization calculation in future work, as well as a more accurate model for the spectral energy distribution of the young pulsar wind nebula. Also, by adopting a relatively low mass fraction of $X_Z \approx 0.1$ of CNO elements (which contribute most of the bound-free opacity in the keV range) we may be underestimating the ionization breakout time and thus overestimating the associated X-ray luminosity if the true mass fraction is higher. On the other hand, asphericity in the ejecta (e.g., along the rotation axis) would reduce the breakout time along directions of lower than average density and introduce a viewing angle dependence to the emission. An extension from an analytical 1D model (used here) to detailed multi-D formulations is indeed necessary to fully characterize the expected X-ray signature from ionization breakout, and possibly solve the current tension between the anticipated versus observed spectral features and their evolution in the magnetar model (e.g., Liu et al. 2017).

6. Summary and Conclusions

We present the results from an extensive systematic survey of X-ray emission from 26 hydrogen-stripped SLSNe in the local universe with *Swift*, *Chandra*, and *XMM*. These data cover the SLSNe-I evolution from ∼days until 2000 days (rest-frame) since explosion, reaching $L_x \sim 10^{40}$ erg s^{-1}. The unprecedented depth of these observations provided the deepest limits on the X-ray emission from SLSNe-I to date and enabled the detection of X-ray emission at the location of the slowly evolving SLSN-I PTF 12dam. The major results from our investigation can be summarized as follows:

1. Superluminous X-ray emission $L_x \sim 10^{45}$ erg s^{-1} of the kind detected at the location of SCP 06F6 is *not* a

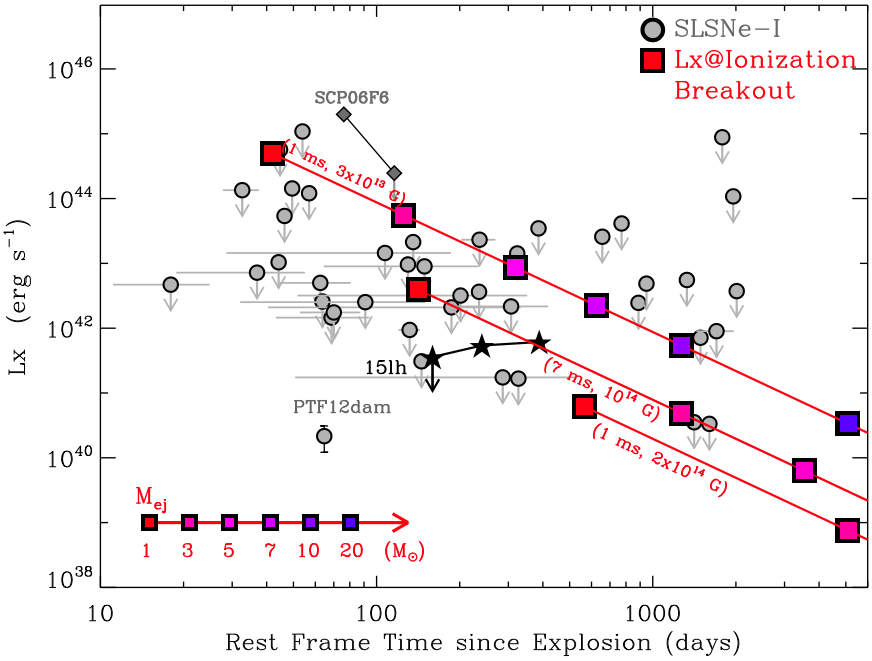

Figure 8. X-ray luminosity at the time of ionization breakout (thick red line) for a variety of representative magnetar parameters, $P = 1$ ms, $B = 3 \times 10^{13}$ G (upper line), $P = 7$ ms, $B = 10^{14}$ G (middle line), $P = 1$ ms, $B = 2 \times 10^{14}$ G (lower line), and for a range of ejecta mass values $M_{\rm ej}$ between 1 and 20 $M_\odot$. These calculations assume an oxygen-dominated ejecta composition ($Z_8 = 1$), $v = 10^9$ cm s^{-1}, $T = 10^5$ K, $X_A = 0.1$. Our limits (gray dots) rule out the fastest spinning magnetars with $P \leqslant 7$ ms, $B \leqslant 10^{14}$ G and small ejecta masses $M_{\rm ej} \leqslant 5\,M_\odot$. However, we are not sensitive to magnetars with $B_{14} \geqslant 2 \times 10^{14}$ G. Gray diamonds: X-ray emission at the location of SCP 06F6 (Levan et al. 2013). Black stars: X-ray emission at the location of ASASSN-15lh (Margutti et al. 2017b).

common trait of SLSNe-I. Superluminous X-ray emission requires peculiar physical conditions that are likely not shared by the majority of SLSNe-I. *If* present, its duration is $\leqslant$2 months at $t < 2000$ days and $\leqslant$ few days at earlier epochs $t < 100$ days.

2. We place sensitive limits on the sub-parsec environments of the SLSNe-I with the deepest observations and constrain the pre-explosion mass-loss histories of the stellar progenitors of SLSNe-I (Figures 5–6). The most sensitive X-ray observations in our sample rule out the densest environments typical of LBV eruptions and type-IIn SNe at distances $d > 10^{16}$ cm. For PTF 12dam, the observations point to a clean environment similar to engine-driven SNe and argue against the extended dense CSM typical of stellar progenitors like RSG. Observations indicate $\dot{M} < 2 \times 10^{-5}\,M_\odot$ yr^{-1}. This result suggests that sustained CSM interaction is unlikely to play a key role in the process that powers the luminous display in some SLSNe-I and that at least some SLSN-I progenitors end their lives as compact stars surrounded by a low-density medium at distances $d > 10^{16}$ cm. Our data do not constrain the properties of the nearby $d < 10^{16}$ cm environment, sculpted by the mass-loss history of the progenitor star in the last $\sim$10 yr before core-collapse.
3. We do not find compelling observational evidence for relativistic outflows in SLSNe-I. SLSNe-I might either be powered by energetic relativistic GRB-like outflows that we did not detect because they were positioned far away from our line of sight ($\theta_{\rm obs} > 30°$), or might harbor failed jets that do not successfully pierce through the stellar envelope. Deep X-ray observations of PTF 12dam rule out even the weakest emission from uncollimated GRB outflows (Figure 7), suggesting that *if* PTF 12dam is a jet-driven explosion, then the jet never successfully broke out from the surface (in close similarity to the relativistic SNe 2009bb and 2012ap). However, the luminous SN 2011kl was found in association with the fully relativistic, fully successful jet of GRB 111209A, suggesting that jet-driven explosions can give rise to SNe more luminous than the average H-stripped core-collapse SNe. We thus propose that, just like H-stripped core-collapse SN, SLSNe-I might also be characterized by a continuum of jet power and central-engine lifetimes.
4. The X-ray ionization breakout is a very sensitive probe of the properties of a hidden magnetar central engine in SLSNe-I. Magnetar central engines that would produce very similar optical/UV displays are instead clearly differentiated in terms of X-ray luminosities and timescales of the ionization breakout (Figures 3–4). Current X-ray observations indicate that *if* a magnetar central engine powers SLSNe-I, then it has to be either associated with a large magnetic field $B_{14} > 2$ G or large ejecta mass ($M_{\rm ej} > 20, 7, 3\,M_\odot$ for $B_{14} = 0.2$, 0.5, 1.0 G).

This X-ray campaign provided constraints on the sub-parsec environment and properties of central engines in SLSNe-I. To further advance our knowledge and understanding of SLSNe-I it is necessary to systematically explore the region of the parameter space with $L_x < 10^{41}$ erg s^{-1} both at very early ($t < 30$ days, rest-frame) and late times ($t > 1000$ days, rest-frame), where the emission from an off-axis relativistic jet, weak uncollimated relativistic outflow or magnetar ionization breakout might be found. This parameter space is almost an entirely uncharted territory of exploration and holds promise for future discoveries.

We thank the referee for constructive criticism and suggestions that helped improve the quality of the paper and the clarity of presentation of our results. We thank A. Kann, K. Murase, and N. Soker for their comments and detailed reading of the manuscript that we posted on the archive. This research has made use of the XRT Data Analysis Software (XRTDAS) developed under the responsibility of the ASI Science Data Center (ASDC), Italy. We acknowledge the use of public data from the *Swift* data archive. This work is partially based on data acquired with the *Swift* GO program 1114109 (PI Margutti). The scientific results reported in this article are partially based on observations made by the *Chandra X-ray Observatory* under program GO6-17052A (PI Margutti), observation IDs 17879, 17880, 17881, 17882, and IDs 13772, 14444, 14446 for PI Pooley. This work is partially based on observations by *XMM-Newton*, IDs 0743110301, 0743110701, 0770380201, 0770380401 (PI Margutti, proposal 74311). D.C. and R.M. acknowledge partial support from programs No. NNX16AT51G and NNX16AT81G provided by NASA through *Swift* Guest Investigator Programs. C.G. acknowledges University of Ferrara for use of the local HPC facility co-funded by the "Large-Scale Facilities 2010" project (grant 7746/2011). Development of the Boxfit code was supported in part by NASA through grant NNX10AF62G issued through the Astrophysics Theory Program and by the NSF through grant AST-1009863. Simulations for BOXFIT version 2 have been carried out in part on the computing facilities of the Computational Center for Particle and Astrophysics (C2PAP) of the research cooperation "Excellence Cluster Universe" in Garching, Germany. G.M. acknowledges the financial support from the UnivEarthS Labex program of Sorbonne Paris Cité (ANR10LABX0023 and ANR11IDEX000502).

Appendix
X-Ray Observations of SLSNe-I

Here we provide the details of the X-ray observations of SLSNe-I in the "bronze" and "iron" samples. Table 5 reports the measured fluxes for the entire sample of 26 SLSNe-I analyzed in this paper. For the non-detections we assume a non-thermal power-law spectrum with a photon index $\Gamma = 2$ and Galactic absorption.

A.1. SN 2009jh/PTF 09cwl

Swift-XRT observed SN 2009jh (Quimby et al. 2011c) on 2009 August 29 until 2016 September 25 ($\delta t = 48$–1961 days rest-frame since explosion). No X-ray source is detected at the location of the supernova. With respect to Levan et al. (2013) we add the late-time data set acquired in 2016.

A.2. PTF 09atu

Swift-XRT observed PTF 09atu (Quimby et al. 2011c) on 2009 August 19 until 2016 October 6 ($\delta t = 49$–1785 days rest-frame since explosion). No X-ray source is detected at the location of the supernova. With respect to Levan et al. (2013) we add the late-time data set acquired in 2016.

A.3. PTF 09cnd

Swift-XRT started observing PTF 09cnd (Quimby et al. 2011c) on 2014 August 8 until October 3 ($\delta t = 1487$–1531 days rest-frame since explosion, exposure time of 26 ks). This data set has been partially presented by Levan et al. (2013). The location of PTF 09cnd was serendipitously observed by *Swift* between 2016 February 4 and September 23 ($\delta t = 1921$–2104 days rest-frame since explosion, exposure time of 62 ks). No X-ray source is detected at the location of the supernova. *XMM* observed the location of PTF 09cnd on 2014 August 8 ($\delta t = 1487$ days rest-frame since explosion). The net exposure time is 27.7 ks (EPIC-pn data). No source is detected and we derive a 3σ count-rate upper limit of 1.5×10^{-3} c s^{-1} (0.3–10 keV), which corresponds to an absorbed (unabsorbed) flux $<3.2 \times 10^{-15}$ erg s^{-1} cm^{-2} ($<3.4 \times 10^{-15}$ erg s^{-1} cm^{-2}).

Table 5
X-Ray Observations of SLSNe-I

SN	t_{START} (MJD)	t_{STOP} (MJD)	Unabsorbed Flux (0.3–10 keV) (10^{-14}erg s^{-1} cm^{-2})	Instrument
SCP 06F6	53949	53949	13.	*XMM*[a]
	54043	54043	<1.40	*Chandra*
PTF 09atu	55062.188	55062.328	<14.50	*Swift*-XRT
	57667.055	57667.055	<89.37	*Swift*-XRT
PTF 09cnd	55061.883	55062.000	<12.02	*Swift*-XRT
	55065.828	55065.945	<12.35	*Swift*-XRT
	55069.016	55069.289	<14.47	*Swift*-XRT
	55073.637	55073.777	<12.43	*Swift*-XRT
	55077.312	55077.594	<17.12	*Swift*-XRT
	55084.012	55084.887	<13.73	*Swift*-XRT
	55097.812	55097.945	<25.94	*Swift*-XRT
	55107.375	55107.453	<22.40	*Swift*-XRT
	57422.016	57422.766	<57.30	*Swift*-XRT

Note.
[a] From Levan et al. (2013).

(This table is available in its entirety in machine-readable form.)

A.4. PTF 10aagc

Swift-XRT observed PTF 10aagc (Yan et al. 2015) on 2010 November 08 ($\delta t = 79$ days rest-frame since explosion). No X-ray source is detected at the location of the supernova.

A.5. SN 2010md/PTF 10hgi

Swift-XRT started observing PTF 10hgi (Inserra et al. 2013) on 2010 July 13 until 2010 July 18 ($\delta t = 61$–66 days rest-frame since explosion). No X-ray source is detected at the location of the supernova as reported by Levan et al. (2013).

A.6. SN 2010gx/CSS100313/PTF 10cwr

Swift-XRT started observing SN 2010gx (Pastorello et al. 2010; Quimby et al. 2011c; Chen et al. 2013; Inserra et al. 2013; Perley et al. 2016) on 2010 March 19 until 2012 May 14 ($\delta t = 19$–659 days rest-frame since explosion). A portion of this data set has been presented by Levan et al. (2013). Here, we add the observations acquired in 2012. No X-ray source is detected at the location of the supernova.

A.7. SN 2010kd

Swift-XRT started observing SN 2010kd (Vinko et al. 2010, 2012) on 2010 November 30 until 2016 June 21 ($\delta t = 120$–1964 days rest-frame since explosion). With respect

to Levan et al. (2013), here we include late-time data acquired in 2014 and 2016. No X-ray source is detected at the location of the supernova.

A.8. SN 2011ke/CSS110406/PTF 11dij

Swift-XRT started observing SN 2011ke (Quimby et al. 2011b; Drake et al. 2013; Perley et al. 2016) on 2011 May 14 until 2012 April 12 ($\delta t = 40$–332 days rest-frame since explosion), as reported by Levan et al. (2013). No X-ray source is detected at the location of the supernova.

The *CXO* serendipitously imaged the sky location of SN 2011ke on 2015 August 28 ($\delta t = 1411$ days rest-frame since explosion, exposure time of 56 ks) and on 2016 April 4 ($\delta t = 1604$ days rest-frame since explosion, exposure time of 59 ks). These data are presented here for the first time. No X-ray source is detected at the location of SN 2011ke and we infer a 3σ count-rate upper limit $<5.4 \times 10^{-5}$ c s^{-1} and $<5.1 \times 10^{-5}$ c s^{-1} in the 0.5–8 keV energy band, for the first and second epoch, respectively. For a non-thermal power-law spectrum with index $\Gamma = 2$ these results translate into unabsorbed 0.3–10 keV flux limits of $<6.4 \times 10^{-16}$ and $<6.0 \times 10^{-16}$ erg s^{-1} cm^{-2}.

A.9. PS1-11bdn

Swift-XRT started observing PS1-11bdn (Lunnan et al. 2014, 2015; Schulze et al. 2018) on 2012 January 11 until 2012 January 28 ($\delta t = 28$–35 days rest-frame since explosion). No X-ray source is detected at the location of the supernova.

A.10. PTF 11rks/SN 2011kg

Swift-XRT started observing PTF 11rks (Quimby et al. 2011a; Inserra et al. 2013; Perley et al. 2016) on 2011 December 30 until 2012 January 15 ($\delta t = 11$–25 days rest-frame since explosion), as reported by Levan et al. (2013). No X-ray source is detected at the location of the supernova.

A.11. SN 2012il/PS1-12fo/CSS120121

Swift-XRT started observing SN 2012il (Drake et al. 2012; Smartt et al. 2012; Inserra et al. 2013; Lunnan et al. 2014) on 2012 February 13 until 2016 June 25 ($\delta t = 44$–1400 days rest-frame since explosion). No X-ray source is detected at the location of the supernova. With respect to Levan et al. (2013) we add the 2016 data set.

A.12. DES15C3hav

Swift-XRT started observing DES15C3hav (Challis et al. 2016) on 2016 June 12 until 2016 September 13 ($\delta t = 202$–269 days rest-frame since explosion). No X-ray source is detected at the location of the supernova.

A.13. iPTF 13ehe

Swift-XRT observed iPTF 13ehe (Wang et al. 2016a; Yan et al. 2015) on 2014 December 23 ($\delta t = 385$ days rest-frame since explosion). No X-ray source is detected at the location of the supernova.

A.14. LSQ 14an

Swift-XRT started observing LSQ 14an (Leget et al. 2014; Jerkstrand et al. 2017; Inserra et al. 2017) on 2014 March 24 until 2014 December 8, with a final observation taken on 2016 August 8 ($\delta t = 196$–949 days rest-frame since explosion). A portion of the data set was presented in Inserra et al. (2017). Here, we present the complete data set of X-ray observations available on LSQ 14an.

A.15. LSQ 14fxj

Swift-XRT started observing LSQ 14fxj (Smith et al. 2014; Schulze et al. 2018) on 2014 October 29 until 2015 June 16 ($\delta t = 64$–234 days rest-frame since explosion). No X-ray source is detected at the location of the supernova.

A.16. LSQ 14mo

Swift-XRT started observing LSQ 14mo (Leloudas et al. 2015a; Chen et al. 2017) on 2014 January 31, with a last observation taken on 2016 July 24 ($\delta t = 52$–774 days rest-frame since explosion). No X-ray source is detected at the location of the supernova.

A.17. CSS140925-005854

Swift-XRT started observing CSS140925-005854 (Campbell et al. 2014; Schulze et al. 2018) on 2014 October 11 until 2015 May 29 ($\delta t = 29$–186 days rest-frame since explosion). No X-ray source is detected at the location of the supernova.

A.18. DES15S2nr

Swift-XRT started observing DES15S2nr (D'Andrea et al. 2015) on 2015 September 25 until 2016 February 15, with another observation acquired on 2016 September 14 ($\delta t = 32$–323 days res-frame since explosion). No X-ray source is detected at the location of the supernova.

A.19. OGLE15qz

Swift-XRT observed OGLE15qz (Kangas et al. 2015; Kostrzewa-Rutkowska et al. 2015) on 2015 November 25 ($\delta t = 54$ days rest-frame since explosion). No X-ray source is detected at the location of the supernova.

A.20. OGLE15sd

Swift-XRT started observing OGLE15sd (Baumont et al. 2015) on 2015 December 8 until 2015 December 9 ($\delta t = 34$–212 days rest-frame since explosion). No X-ray source is detected at the location of the supernova.

A.21. PS16aqv

Swift-XRT started observing PS16aqv (Chornock et al. 2016) on 2016 March 9 until 2016 June 10 ($\delta t = 53$–131 days rest-frame since explosion). No X-ray source is detected at the location of the supernova.

A.22. PS16op

Swift-XRT observed PS16op (Dimitriadis et al. 2016) on 2016 January 20 ($\delta t = 57$ days rest-frame since explosion). No X-ray source is detected at the location of the supernova.

ORCID iDs

R. Margutti https://orcid.org/0000-0003-4768-7586
B. D. Metzger https://orcid.org/0000-0002-4670-7509
C. Guidorzi https://orcid.org/0000-0001-6869-0835
G. Migliori https://orcid.org/0000-0003-0216-8053
D. Milisavljevic https://orcid.org/0000-0002-0763-3885
E. Berger https://orcid.org/0000-0002-9392-9681
M. Nicholl https://orcid.org/0000-0002-2555-3192
R. Lunnan https://orcid.org/0000-0001-9454-4639
A. Kamble https://orcid.org/0000-0003-0861-5168
M. Modjaz https://orcid.org/0000-0001-7132-0333

References

Angus, C. R., Levan, A. J., Perley, D. A., et al. 2016, MNRAS, 458, 84
Barbary, K., Dawson, K. S., Tokita, K., et al. 2009, ApJ, 690, 1358
Baumont, S., Le Guillou, L., Le Breton, R., et al. 2015, ATel, 8369
Benetti, S., Nicholl, M., Cappellaro, E., et al. 2014, MNRAS, 441, 289
Berger, E., Kulkarni, S. R., & Chevalier, R. A. 2002, ApJL, 577, L5
Bersten, M. C., Benvenuto, O. G., Orellana, M., & Nomoto, K. 2016, ApJL, 817, L8
Björnsson, C.-I., & Fransson, C. 2004, ApJ, 605, 823
Campbell, H., Walton, N., Blagorodnova, N., et al. 2014, ATel, 6524
Chakraborti, S., Soderberg, A., Chomiuk, L., et al. 2015, ApJ, 805, 187
Challis, P., Kirshner, R., Mandel, K., et al. 2016, ATel, 8952
Chatzopoulos, E., Wheeler, J. C., Vinko, J., et al. 2016, ApJ, 828, 94
Chen, T.-W., Nicholl, M., Smartt, S. J., et al. 2017, A&A, 602, A9
Chen, T.-W., Smartt, S. J., Bresolin, F., et al. 2013, ApJL, 763, L28
Chen, T.-W., Smartt, S. J., Jerkstrand, A., et al. 2015, MNRAS, 452, 1567
Chevalier, R. A., & Fransson, C. 2006, ApJ, 651, 381
Chevalier, R. A., & Irwin, C. M. 2011, ApJL, 729, L6
Chomiuk, L., Chornock, R., Soderberg, A. M., et al. 2011, ApJ, 743, 114
Chornock, R., Bhirombhakdi, K., Katebi, R., et al. 2016, ATel, 8790
Coppejans, D. L., Margutti, R., Guidorzi, C., et al. 2018, ApJ, 856, 56
Corsi, A., Ofek, E. O., Gal-Yam, A., et al. 2014, ApJ, 782, 42
Crowther, P. A. 2007, ARA&A, 45, 177
Dai, L., McKinney, J. C., & Miller, M. C. 2015, ApJL, 812, L39
Dai, Z. G., Wang, S. Q., Wang, J. S., Wang, L. J., & Yu, Y. W. 2016, ApJ, 817, 132
D'Andrea, C., Smith, M., Sullivan, M., et al. 2015, ATel, 8092
de Jager, C., Nieuwenhuijzen, H., & van der Hucht, K. A. 1988, A&AS, 72, 259
Dimitriadis, G., Firth, R., Frohmaier, C., et al. 2016, ATel, 8555
Dong, S., Shappee, B. J., Prieto, J. L., et al. 2016, Sci, 351, 257
Drake, A. J., Djorgovski, S. G., Mahabal, A. A., et al. 2012, ATel, 3873
Drake, A. J., Djorgovski, S. G., Mahabal, A. A., et al. 2013, CBET, 3460, 1
Drout, M. R., Milisavljevic, D., Parrent, J., et al. 2016, ApJ, 821, 57
Fransson, C., & Björnsson, C.-I. 1998, ApJ, 509, 861
Gal-Yam, A. 2012, Sci, 337, 927
Gal-Yam, A., Mazzali, P., Ofek, E. O., et al. 2009, Natur, 462, 624
Gänsicke, B. T., Levan, A. J., Marsh, T. R., & Wheatley, P. J. 2009, ApJL, 697, L129
Godoy-Rivera, D., Stanek, K. Z., Kochanek, C. S., et al. 2017, MNRAS, 466, 1428
Greiner, J., Mazzali, P. A., Kann, D. A., et al. 2015, Natur, 523, 189
Inserra, C., Nicholl, M., Chen, T.-W., et al. 2017, MNRAS, 468, 4642
Inserra, C., Smartt, S. J., Jerkstrand, A., et al. 2013, ApJ, 770, 128
Jerkstrand, A., Smartt, S. J., Inserra, C., et al. 2017, ApJ, 835, 13
Kalberla, P. M. W., Burton, W. B., Hartmann, D., et al. 2005, A&A, 440, 775
Kamble, A., Margutti, R., Soderberg, A. M., et al. 2016, ApJ, 818, 111
Kamble, A., Soderberg, A. M., Chomiuk, L., et al. 2014, ApJ, 797, 2
Kangas, T., Dennefeld, M., Harmanen, J., et al. 2015, ATel, 8296
Kann, D. A., Schady, P., Olivares, E. F., et al. 2016, arXiv:1606.06791
Kasen, D., & Bildsten, L. 2010, ApJ, 717, 245
Kostrzewa-Rutkowska, Z., Wyrzykowski, L., Kozlowski, S., et al. 2015, ATel, 8314
Kouveliotou, C., Woosley, S. E., Patel, S. K., et al. 2004, ApJ, 608, 872
Kozyreva, A., Hirschi, R., Blinnikov, S., & den Hartogh, J. 2016, MNRAS, 459, L21
Krauss, M. I., Soderberg, A. M., Chomiuk, L., et al. 2012, ApJL, 750, L40
Lazzati, D., Morsony, B. J., Blackwell, C. H., & Begelman, M. C. 2012, ApJ, 750, 68
Leget, P.-F., Guillou, L. L., Fleury, M., et al. 2014, ATel, 5718
Leloudas, G., Fraser, M., Stone, N. C., et al. 2016, NatAs, 1, 2, [Corrigendum: NatAs, 2016, 1, 34]
Leloudas, G., Patat, F., Maund, J. R., et al. 2015a, ApJL, 815, L10
Leloudas, G., Schulze, S., Krühler, T., et al. 2015b, MNRAS, 449, 917
Levan, A. J., Read, A. M., Metzger, B. D., Wheatley, P. J., & Tanvir, N. R. 2013, ApJ, 771, 136
Liu, Y.-Q., Modjaz, M., & Bianco, F. B. 2017, ApJ, 845, 85
Lunnan, R., Chornock, R., Berger, E., et al. 2014, ApJ, 787, 138
Lunnan, R., Chornock, R., Berger, E., et al. 2015, ApJ, 804, 90
Lunnan, R., Chornock, R., Berger, E., et al. 2016, ApJ, 831, 144
Margalit, B., Metzger, B. D., Thompson, T. A., Nicholl, M., & Sukhbold, T. 2018, MNRAS, 475, 2659
Margutti, R., Kamble, A., Milisavljevic, D., et al. 2017a, ApJ, 835, 140
Margutti, R., Metzger, B. D., Chornock, R., et al. 2017b, ApJ, 836, 25
Margutti, R., Milisavljevic, D., Soderberg, A. M., et al. 2014, ApJ, 797, 107
Margutti, R., Soderberg, A. M., Chomiuk, L., et al. 2012, ApJ, 751, 134
Margutti, R., Soderberg, A. M., Wieringa, M. H., et al. 2013a, ApJ, 778, 18
Margutti, R., Zaninoni, E., Bernardini, M. G., et al. 2013b, MNRAS, 428, 729
Marshall, J. R., van Loon, J. T., Matsuura, M., et al. 2004, MNRAS, 355, 1348
Massey, P., Neugent, K. F., & Morrell, N. 2015, ApJ, 807, 81
Mazzali, P. A., Valenti, S., Della Valle, M., et al. 2008, Sci, 321, 1185
Metzger, B. D., Margalit, B., Kasen, D., & Quataert, E. 2015, MNRAS, 454, 3311
Metzger, B. D., & Piro, A. L. 2014, MNRAS, 439, 3916
Metzger, B. D., Vurm, I., Hascoët, R., & Beloborodov, A. M. 2014, MNRAS, 437, 703
Milisavljevic, D., Soderberg, A. M., Margutti, R., et al. 2013, ApJL, 770, L38
Mineo, S., Gilfanov, M., & Sunyaev, R. 2012, MNRAS, 426, 1870
Nicholl, M., Berger, E., Margutti, R., et al. 2016a, ApJL, 828, L18
Nicholl, M., Berger, E., Margutti, R., et al. 2017, ApJL, 835, L8
Nicholl, M., Berger, E., Smartt, S. J., et al. 2016b, ApJ, 826, 39
Nicholl, M., Smartt, S. J., Jerkstrand, A., et al. 2013, Natur, 502, 346
Nicholl, M., Smartt, S. J., Jerkstrand, A., et al. 2014, MNRAS, 444, 2096
Ofek, E. O., Cameron, P. B., Kasliwal, M. M., et al. 2007, ApJL, 659, L13
Ofek, E. O., Zoglauer, A., Boggs, S. E., et al. 2014, ApJ, 781, 42
Pastorello, A., Smartt, S. J., Botticella, M. T., et al. 2010, ApJL, 724, L16
Perley, D. A., Quimby, R. M., Yan, L., et al. 2016, ApJ, 830, 13
Pian, E., Amati, L., Antonelli, L. A., et al. 2000, ApJ, 536, 778
Quimby, R. M., Gal-Yam, A., Arcavi, I., et al. 2011a, ATel, 3841
Quimby, R. M., Kulkarni, S. R., Kasliwal, M. M., et al. 2011c, Natur, 474, 487
Quimby, R. M., Sternberg, A., & Matheson, T. 2011b, ATel, 3344
Romano, P., Guidorzi, C., Segreto, A., Ducci, L., & Vercellone, S. 2014, A&A, 572, A97
Roming, P. W. A., Pritchard, T. A., Brown, P. J., et al. 2009, ApJL, 704, L118
Ryder, S. D., Sadler, E. M., Subrahmanyan, R., et al. 2004, MNRAS, 349, 1093
Schulze, S., Krühler, T., Leloudas, G., et al. 2018, MNRAS, 473, 1258
Sironi, L., Keshet, U., & Lemoine, M. 2015, SSRv, 191, 519
Smartt, S. J., Wright, D., Valenti, S., et al. 2012, ATel, 3918
Smith, M., Firth, R., Dimitriadis, G., et al. 2014, ATel, 6739
Smith, N. 2014, ARA&A, 52, 487
Smith, N., & McCray, R. 2007, ApJL, 671, L17
Smith, N., & Owocki, S. P. 2006, ApJL, 645, L45
Soderberg, A. M., Berger, E., Page, K. L., et al. 2008, Natur, 453, 469
Soderberg, A. M., Brunthaler, A., Nakar, E., Chevalier, R. A., & Bietenholz, M. F. 2010a, ApJ, 725, 922
Soderberg, A. M., Chakraborti, S., Pignata, G., et al. 2010b, Natur, 463, 513
Soderberg, A. M., Kulkarni, S. R., Berger, E., et al. 2005, ApJ, 621, 908
Soderberg, A. M., Kulkarni, S. R., Nakar, E., et al. 2006a, Natur, 442, 1014
Soderberg, A. M., Nakar, E., Berger, E., & Kulkarni, S. R. 2006b, ApJ, 638, 930
Soker, N. 2017, RAA, 17, 113
Sukhbold, T., & Woosley, S. E. 2016, ApJL, 820, L38
Thöne, C. C., de Ugarte Postigo, A., García-Benito, R., et al. 2015, MNRAS, 451, L65
van Dyk, S. D., Weiler, K. W., Sramek, R. A., Rupen, M. P., & Panagia, N. 1994, ApJL, 432, L115
van Eerten, H., van der Horst, A., & MacFadyen, A. 2012, ApJ, 749, 44
van Loon, J. T., Cioni, M.-R. L., Zijlstra, A. A., & Loup, C. 2005, A&A, 438, 273
van Putten, M. H. P. M., & Della Valle, M. 2017, MNRAS, 464, 3219
Vinko, J., Zheng, W., Pandey, S. B., et al. 2012, AAS Meeting, 219, 436

Vinko, J., Zheng, W., Romadan, A., et al. 2010, CBET, 2556
Vreeswijk, P. M., Leloudas, G., Gal-Yam, A., et al. 2017, ApJ, 835, 58
Wang, S. Q., Liu, L. D., Dai, Z. G., Wang, L. J., & Wu, X. F. 2016a, ApJ, 828, 87
Wang, S. Q., Liu, L. D., Dai, Z. G., Wang, L. J., & Wu, X. F. 2016b, ApJ, 828, 87
Watson, D., Hjorth, J., Levan, A., et al. 2004, ApJL, 605, L101
Weiler, K. W., Panagia, N., Montes, M. J., & Sramek, R. A. 2002, ARA&A, 40, 387
Woosley, S. E. 2010, ApJL, 719, L204
Xu, D., Watson, D., Fynbo, J., et al. 2008, in COSPAR Meeting 37, 37th COSPAR Scientific Assembly, 3512
Yan, L., Lunnan, R., Perley, D. A., et al. 2017, ApJ, 848, 6
Yan, L., Quimby, R., Ofek, E., et al. 2015, ApJ, 814, 108